Flexible Dimethylsilylene Bridges in Silicon Quantum Dot-Anthracene Adducts Promote Triplet Energy Transfer

Sina G. Lewis[2#], Kefu Wang[3#], Nhien Q. Nguyen[1#], Aracely Gonzalez[1], Honghao Wang[4], Timothy C. Siu[1], Lorenzo Mangolini[5], Sean T. Roberts[4], Timothy A. Su[1*], Joel David Eaves[6*] & Ming Lee Tang[3*]

[1]*Department of Chemistry, University of California Riverside, Riverside, USA.*
[2]*Department of Physics, University of Colorado Boulder, Boulder, USA.*
[3]*Department of Chemistry, University of Utah, Salt Lake City, USA.*
[4]*Department of Chemistry, The University of Texas at Austin, Austin, USA*
[5]*Department of Mechanical Engineering, University of California Riverside, Riverside, USA.*
[6]*Department of Chemistry, University of Colorado Boulder, Boulder, USA.*
[#]*These authors contributed equally*

Table of Contents

I. Surface Functionalization of Silicon Quantum Dots (Si QDs)

Si QDs partially functionalized with 1-dodecane (Si:dodecane) were synthesized using a non-thermal plasma. After synthesis, these QDs were transferred to a glovebox under a nitrogen environment and dissolved in toluene. The resulting concentrated Si:dodecane solution was then diluted with mesitylene until its optical density at 488 nm was ~1.2 in a 1 cm pathlength cuvette. To prepare Si QDs with different anthracene surface concentrations, varying amounts of silane anthracene precursors ($HSiMe_2A$, $H[SiMe_2]_2A$, $H[SiMe_2]_3A$, and $H[SiMe_2]_4A$) were used during reaction with Si QDs, while di-*tert*butylperoxide (DTBP) was used as the radical initiator for the above reaction. All ingredients needed to functionalize Si QDs via radical initiation were added to a 4 mL vial with a Teflon cap, which was then sealed and heated to 145 ºC for three hours while undergoing constant stirring. This induces the attachment of $[SiMe_2]_nA$ (n = 1 – 4) to Si QDs (labeled as Si:$[SiMe_2]_nA$, n = 1 – 4), respectively. After the reaction, methanol was added to the clear yellow mixture (methanol:mixture = 2:1 by volume) to precipitate out the QDs by centrifuging at 12,000 rpm for 30 mins. The precipitated QDs were then redispersed in 1.5 mL of toluene, followed by addition of 3 mL of methanol and centrifuged at 12,000 rpm for 20 mins again. This cleaning procedure was repeated three times and the final Si:$[SiMe_2]_nA$ (n = 1 – 4) samples were redispersed in toluene for future use.

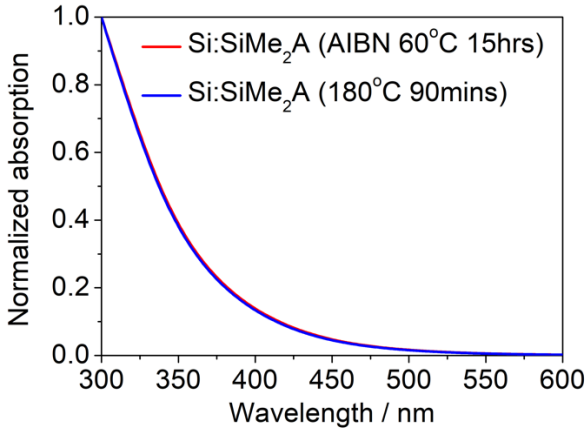

Figure S1: Electronic absorption spectra after removing unaffixed anthracene ligands post-reaction using the AIBN radical initiator method and high temperature thermal methods for functionalizing Si QDs with $HSiMe_2A$. The lack of vibrational fine structure peaks corresponding to anthracene near 400 nm indicates these methods failed to attach $HSiMe_2A$ to the QD surface.

For photon upconversion measurements, Si:$[SiMe_2]_nA$ (n = 1 – 4) solutions were diluted with toluene to give an optical density of ~0.1 at 488 nm in a 1 cm pathlength cuvette. At that point, 9,10-diphenylanthacene (DPA) was added to the Si:$[SiMe_2]_nA$ (n = 1 – 4) solution to give a final DPA concentration of 5.2 mM. The resulting mixture was transferred into a 10 mm × 10 mm quartz cuvette and sealed with an air-tight Teflon cap in a glovebox before taking out for testing.

	Si QDs (OD_{488} = 1.2)	$H[SiMe_2]_nA$ (n = 1 – 4)	DTBP: $H[SiMe_2]_nA$ (n = 1 – 4) (molar ratio)
Sample 1	200 µL	0.5 mg	0.5:1
Sample 2	200 µL	1.0 mg	0.5:1
Sample 3	200 µL	2.0 mg	0.5:1
Sample 4	200 µL	5.0 mg	0.5:1

Table S1: Synthetic parameters for Si:$[SiMe_2]_nA$ (n = 1 – 4) hybrids with different anthracene loadings using the DTBP radical initiator in dry and degassed mesitylene. A total volume of 0.3 mL including mesitylene was used for each reaction.

II. Photophysical Characterization

1. Quantification of the Number of Surface-bound Anthracene Molecules

The average number of anthracene molecules that bind to the surfaces of Si:$[SiMe_2]_n$A (n = 1 – 4) was assessed using absorption spectroscopy. Absorption spectra of anchored anthracene in Si:$[SiMe_2]_n$A (n = 1 – 4) show vibronic progressions in the range of 340 – 460 nm that arise from surface-bound anthracene molecules. The amplitude of these features can be obtained by subtracting the absorption spectrum of Si:dodecane from that of Si:$[SiMe_2]_n$A (n = 1 – 4) samples. Prior to subtraction, to normalize for variations in the Si QD concentration of each sample, the spectrum of the Si:dodecane background was scaled to match that of Si:$[SiMe_2]_n$A (n = 1 – 4) in the spectral region between 550 – 700 nm wherein attached anthracenes do not absorb light. Taking Si:$SiMe_2$A as an example, we can compare this background subtracted spectrum to molar extinction coefficients for $HSiMe_2$A to determine the concentration of surface-bound $SiMe_2$A molecules in solution while the Si QD concentration can be determined using reported extinction spectra. This yields the following expression for $\langle N_{SiMe2A} \rangle$, the average number of surface-bound $SiMe_2$A molecules:

$$\langle N_{SiMe2A} \rangle = \frac{[\mathrm{SiMe_2A}]}{[Si\ QD]} = \frac{abs_{Si:SiMe_2A,404nm} - abs_{Si:dodecane,404nm} \frac{\langle abs_{Si:SiMe_2A} \rangle}{\langle abs_{Si:dodecane} \rangle}}{\varepsilon_{HSiMe_2A,390nm}} \Bigg/ \frac{abs_{Si:SiMe_2A,488nm}}{\varepsilon_{Si\ QD,488nm}} \quad (S1)$$

Here, $\langle abs_{Si:SiMe_2A} \rangle / \langle abs_{Si:dodecane} \rangle$ denotes the normalization value used to match absorption spectra of Si:$SiMe_2$A and Si:dodecane across the 550 – 700 nm spectral range, $\varepsilon_{Si\ QD,488nm}$ is the molar extinction coefficient of the ~3.1 nm diameter Si QDs we employ at 488 nm (10,000 $M^{-1}cm^{-1}$)[1], and $\varepsilon_{HSiMe_2A,390nm}$ corresponds to the molar extinction coefficient of $HSiMe_2$A at 390 nm obtained by Beer's law below, which corresponds to the maximum of its 0-0 vibronic transition. Note, in comparing the extinction spectra of $HSiMe_2$A to background-subtracted spectra of Si:$SiMe_2$A, we account for a 14 nm red shift in the absorption maxima of the latter's 0-0 transition that results from the difference in the dielectric environments felt by $HSiMe_2$A molecules dissolved in toluene and $SiMe_2$A molecules bound to the surface of Si QDs.

A similar approach was used to determine $\langle N_{[SiMe_2]_2A} \rangle$, $\langle N_{[SiMe_2]_3A} \rangle$, and $\langle N_{[SiMe_2]_4A} \rangle$, the number of anthracene molecules attached to the surface of Si:$[SiMe_2]_2$A, Si:$[SiMe_2]_3$A, and Si:$[SiMe_2]_4$A, respectively.

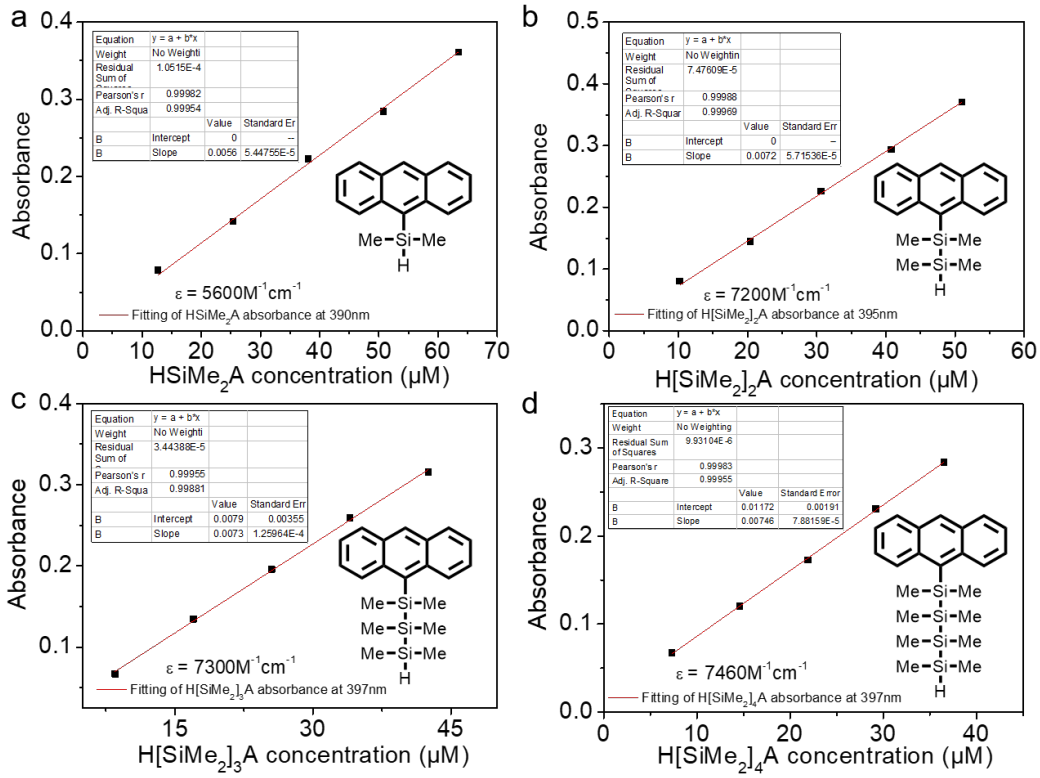

Figure S2: Beer's law plots used to determine molar extinction coefficients for $HSiMe_2A$, $H[SiMe_2]_2A$, $H[SiMe_2]_3A$, and $H[SiMe_2]_4A$.

2. Photon Upconversion Quantum Efficiency Measurements

Photon upconversion measurements were performed using a 488 nm OBIS Coherent laser as an excitation source and an Andor Kymera 328 spectrometer for detection of upconverted light. Emitted photoluminescence (PL) was filtered through a ThorLabs 488 nm notch filter to remove scattered excitation light before being received by the spectrometer. For each upconversion measurement, the system was calibrated using diluted 9,10-diphenylanthracene (DPA) in toluene as an emission reference (PLQY = 90%). The upconversion quantum yield (UCQY) was determined using the following expression:

$$\phi_{UC} = 2 \times \phi_{ref} \times \frac{photons\ absorbed\ by\ reference}{photons\ absorbed\ by\ upconversion\ solution} \times \frac{upconversion\ PL}{reference\ PL} \qquad (S2a)$$

$$= 2 \times \phi_{ref} \times \frac{1 - 10^{-OD_{ref}}}{1 - 10^{-OD_{Si\ QD}}} \times \frac{n_{upc}^2}{n_{ref}^2} \times \frac{[Area]_{upc}}{[Area]_{ref}} \qquad (S2b)$$

where ϕ_{ref} is the PLQY of reference DPA, n_{upc} and n_{ref} are the refractive indices of the solvents for the upconversion and reference solutions (both are toluene), $[Area]_{upc}$ and $[Area]_{ref}$ are the integrated areas of the fluorescence peaks corresponding to upconverted and DPA reference emission, respectively, and OD_{ref} and $OD_{Si\ QD}$ denote the absorbance of reference DPA and Si QDs at the laser excitation wavelength. Note, this expression includes a factor of 2 to normalize the maximum achievable UCQY to a value of 100%.

3. Correcting Photon Upconversion Efficiency Yields to Account for Reabsorption of Emitted Light

For photon upconversion measurements, if the emitter concentration is high, this can lead to a strong reabsorption of the upconverted light by emitter molecules in solution (inner filter effect), thereby lowering

the upconversion efficiency. To assess how much this inner filter effect impacts measured UCQY values, we have matched upconverted emission spectra with those measured by exciting the emitters directly in low-concentration solutions wherein negligible reabsorption of emitted light occurs. Negligible reabsorption in these low-concentration reference solutions was confirmed by verifying a lack of dependence of their emission lineshapes on emitter concentration. Emission spectra measured from upconversion samples were normalized to those of the low-concentration (10 μM) references by matching spectra along their long-wavelength edges wherein emitters show no appreciable absorption. This allowed us to compute the ratio of the integrated area of the photon upconversion lineshape and the intrinsic emission lineshape of the emitter, which was then used to scale measured UCQYs to account for the reabsorption of emitted light. Taking into account this inner filter effect, UCQYs of Si:$SiMe_2$A:DPA, Si:$[SiMe_2]_2$A:DPA, Si:$[SiMe_2]_3$A:DPA, and Si:$[SiMe_2]_4$A:DPA systems were computed to adopt maximum values of 6.2 ± 0.4%, 3.4 ± 0.1%, 4.1 ± 0.2%, and 3.9 ± 0.1%, respectively. The UCQYs reported in the main paper are all corrected values.

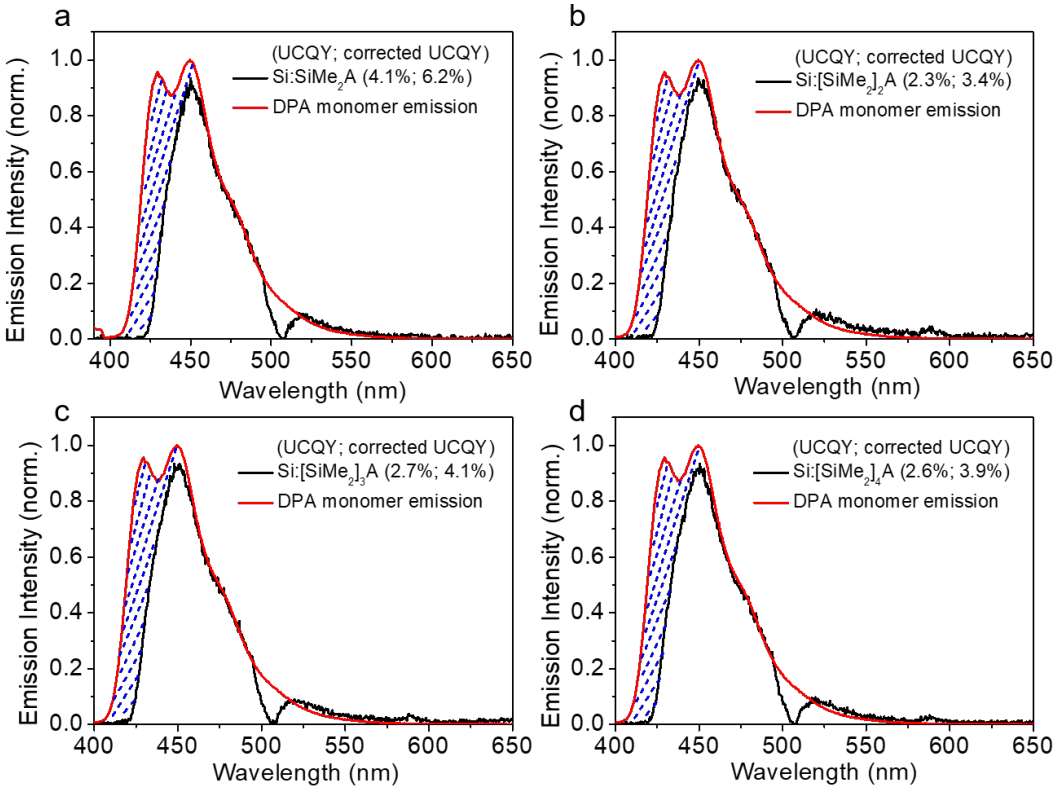

Figure S3: (a) PL spectra of Si:$SiMe_2$A:DPA (black solid line, $\langle N_{SiMe_2A} \rangle$ = 2.7, 5.2 mM DPA, excited at 488 nm) and low-concentration DPA (red dashed line, excited at 375 nm, 10 μM DPA in toluene). (b) PL spectra of Si:$[SiMe_2]_2$A:DPA (black solid line, $\langle N_{[SiMe_2]_2A} \rangle$ = 1.5) and low-concentration DPA. (c) PL spectra of Si:$[SiMe_2]_3$A:DPA (black solid line, $\langle N_{[SiMe_2]_3A} \rangle$ = 1.3) and low-concentration DPA. (d) PL spectra of Si:$[SiMe_2]_4$A:DPA (black solid line, $\langle N_{[SiMe_2]_4A} \rangle$ = 1.6) and low-concentration DPA.

4. Triplet Sensitization of Free H$[SiMe_2]_n$A (n = 1 – 4) Molecules

To identify the triplet absorption spectrum of H$[SiMe_2]_n$A (n = 1 – 4) monomers, we performed triplet sensitization experiments using platinum octaethylporphyrin (PtOEP). Mixtures of PtOEP and either $HSiMe_2$A, H$[SiMe_2]_2$A, H$[SiMe_2]_3$A, or H$[SiMe_2]_4$A in toluene were prepared and placed into sealed cuvettes. Photoexcitation of PtOEP's Q-band at 532 nm generates PtOEP's lowest excited singlet state, which rapidly intersystem crosses to its triplet state on a ~165 fs timescale[2]. Since the energy of PtOEP's lowest triplet state is 1.9 eV[3], which is higher than that of $HSiMe_2$A, H$[SiMe_2]_2$A, H$[SiMe_2]_3$A, and

$H[SiMe_2]_4A$ (~1.8 eV), diffusional collisions between photoexcited PtOEP and $H[SiMe_2]_nA$ (n = 1 – 4) monomers can result in triplet energy transfer from PtOEP to $H[SiMe_2]_nA$ (n = 1 – 4), thus allowing us to identify the triplet absorption spectra of $HSiMe_2A$, $H[SiMe_2]_2A$, $H[SiMe_2]_3A$, and $H[SiMe_2]_4A$ (**Figure S4**).

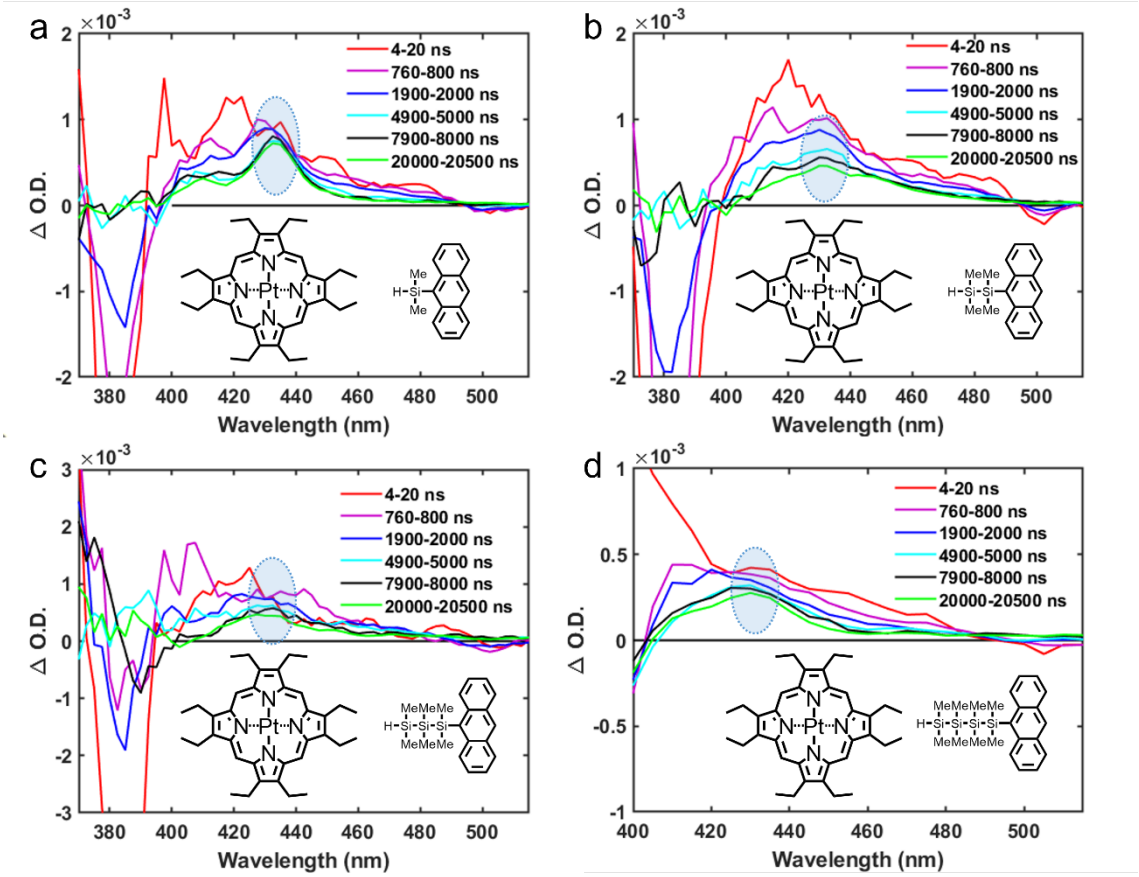

Figure S4: Transient absorption (TA) spectra tracking triplet photosensitization of (a) $HSiMe_2A$, (b) $H[SiMe_2]_2A$, (c) $H[SiMe_2]_3A$, and (d) $H[SiMe_2]_4A$ by PtOEP following excitation of PtOEP by a 532 nm laser.

5. Femtosecond Dynamics of Si:$[SiMe_2]_nA$

Figure S5 shows transient absorption (TA) spectra of Si:dodecane and the four Si:$[SiMe_2]_nA$ systems we investigate that were recorded over time delays of a few hundred femtoseconds up to 1.5 ns following photoexcitation of each sample at 400 nm. A background signal that arises from the solvent (toluene) has been subtracted from this data by measuring a TA spectrum of neat toluene and scaling it to match features seen that arise from the solvent at short time delays. At early delay times, TA spectra of all five samples show a prominent induced absorption signal across the visible spectrum whose intensity profile is dominated by two prominent bands seen at wavelengths below 400 nm and greater than 600 nm. Over the course of ~50 ps, we find these features relax and give rise to a spectrally flat induced absorption across the visible region. This spectral evolution is similar for all five samples, which leads us to assign it to excitons relaxing through the manifold of excited states that are internal to the Si QDs to reach their lowest-energy excited state. No transient signals attributable to the triplet state of the anthracene ligands are observed on sub-nanosecond timescales, further supporting our assignment of these dynamics to ones internal to the Si QDs.

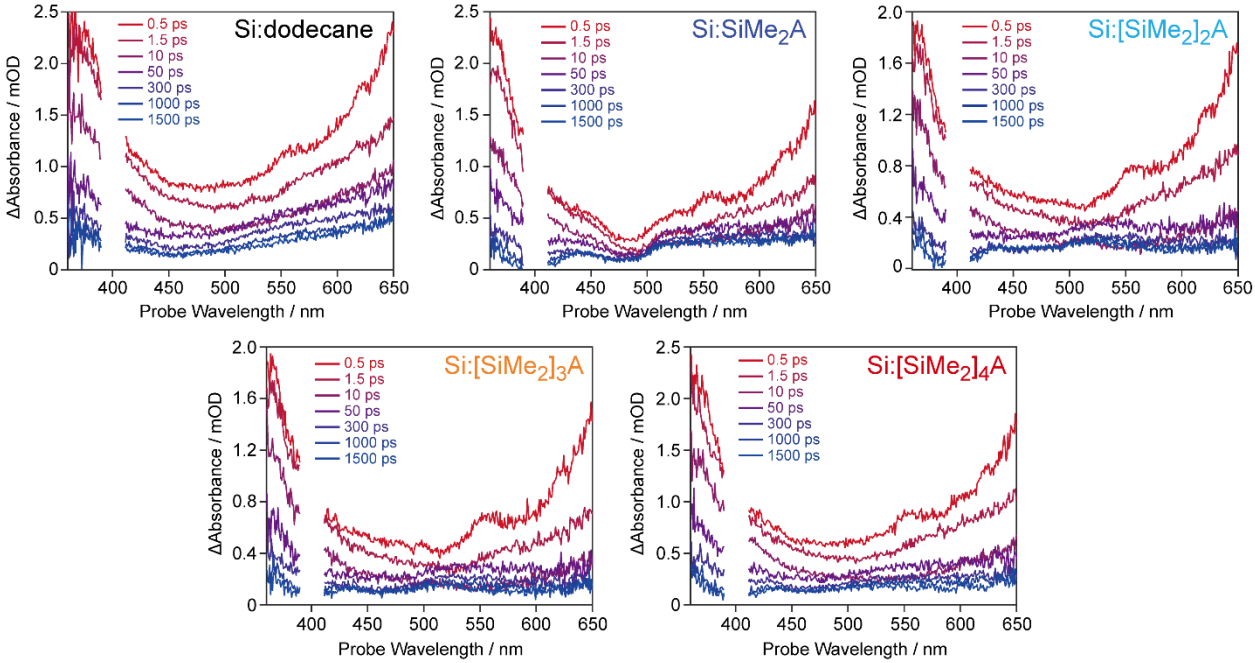

Figure S5: TA spectra of Si:dodecane, Si:$SiMe_2$A, Si:$[SiMe_2]_2$A, Si:$[SiMe_2]_3$A, and Si:$[SiMe_2]_4$A recorded over femtosecond-to-nanosecond time delays following photoexcitation of each sample at 400 nm. The observed spectral dynamics are assigned to exciton cooling within the Si QDs following photoexcitation. These dynamics are largely found to be identical across each of these samples. No evidence of triplet transfer to anthracene ligands is seen on sub-nanosecond timescales.

6. Determination of Triplet Transfer Rates for Si:$[SiMe_2]_n$A

In **Figure 4** of the main text, we highlight the growth of an induced absorption band peaked near 450 nm in TA spectra of Si:$SiMe_2$A, Si:$[SiMe_2]_2$A, Si:$[SiMe_2]_3$A, and Si:$[SiMe_2]_4$A that we assign to population of the anthracene triplet state as a result of energy transfer from a photoexcited Si QD. In principle, the growth of this signal can be directly fit to an exponential rise, but doing so accurately is complicated as the TA signal in this spectral range overlaps with a background induced absorption signal from excited charge carriers within the Si QDs. Thus, to remove this background, we apply a procedure we have successfully used in prior work to suppress contributions to TA spectra that arise from photoexcited Si QDs[1, 4]. This procedure takes advantage of the fact that the anthracene triplet state shows no appreciable absorption at wavelengths extending from 700 – 900 nm whereas charge carriers within Si QDs show a prominent signal in this range. Thus, at each pump-probe time delay, we subtract from TA spectra of Si:$SiMe_2$A, Si:$[SiMe_2]_2$A, Si:$[SiMe_2]_3$A, and Si:$[SiMe_2]_4$A a TA spectrum of Si:dodecane measured at the same time delay that has been scaled to match the spectra of Si:$SiMe_2$A, Si:$[SiMe_2]_2$A, Si:$[SiMe_2]_3$A, and Si:$[SiMe_2]_4$A in the spectral range of 700 – 900 nm where anthracene does not absorb.

Figure S6 shows TA spectra of each of these four samples before and after this background subtraction procedure. For each sample, we find this procedure removes well the prominent induced absorption band that extends from 600 to > 900 nm that arises from excited charge carriers within Si QDs, yielding a TA spectrum that is largely flat in this spectral range. For each sample, two prominent features remain, an induced absorption band peaked near ~450 nm that we assign to the anthracene triplet state and a negative band near ~415 nm that arises from depletion of the anthracene ground state. We note that for Si:$[SiMe_2]_2$A in particular, this ground state bleaching feature is obscured in raw TA spectra (**Figure S6c**) but becomes readily apparent following the removal of induced absorption features that stem from excited carriers within Si QDs (**Figure S6d**).

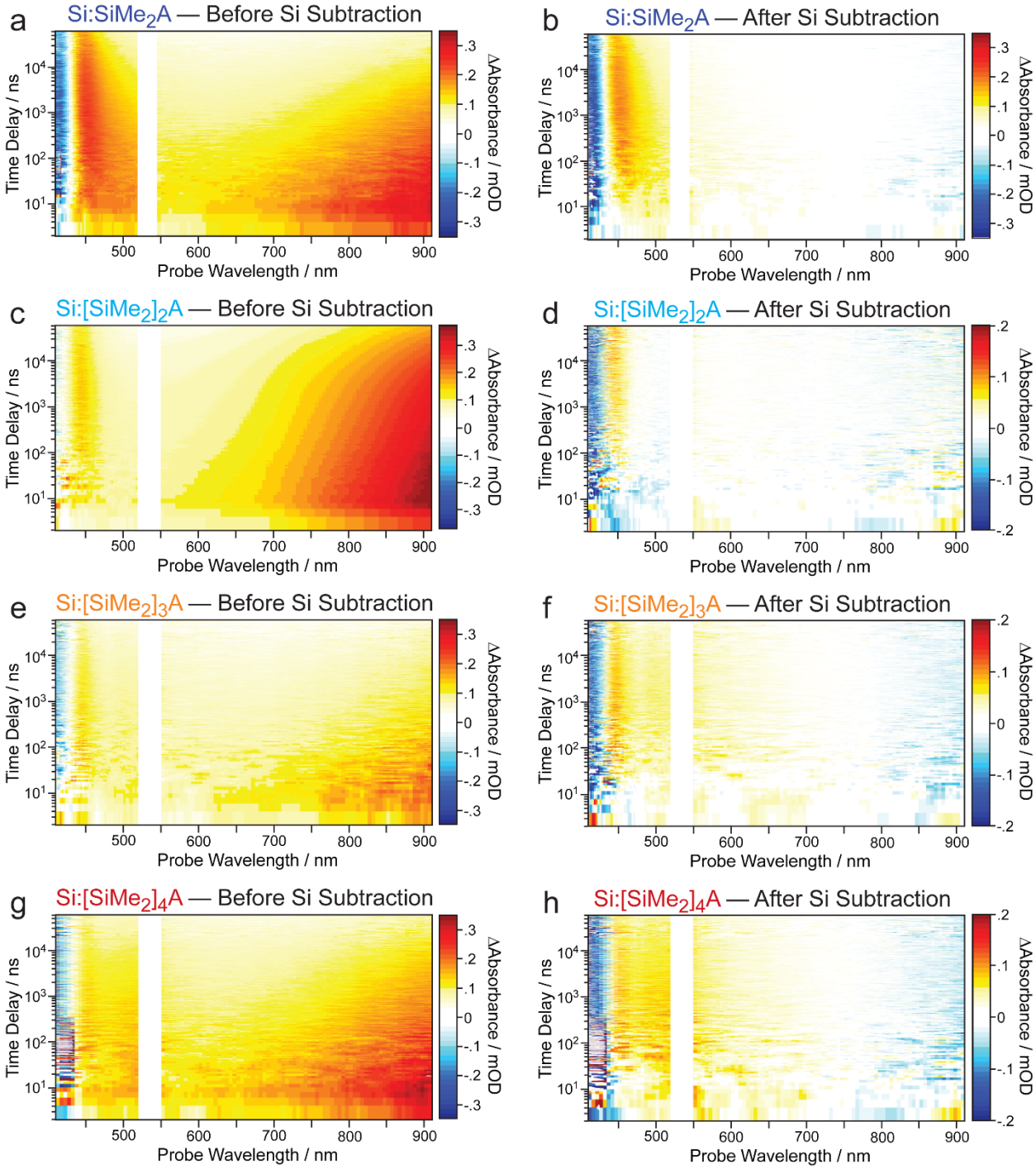

Figure S6: TA spectra of Si:SiMe$_2$A (a & b), Si:[SiMe$_2$]$_2$A (c & d), Si:[SiMe$_2$]$_3$A (e & f), and Si:[SiMe$_2$]$_4$A (g & h) before (left column) and after (right column) removal of the Si QD induced absorption background. Data recorded near 532 nm is omitted due to pump scatter. Data reported for Si:SiMe$_2$A originally appeared in Ref. 4.

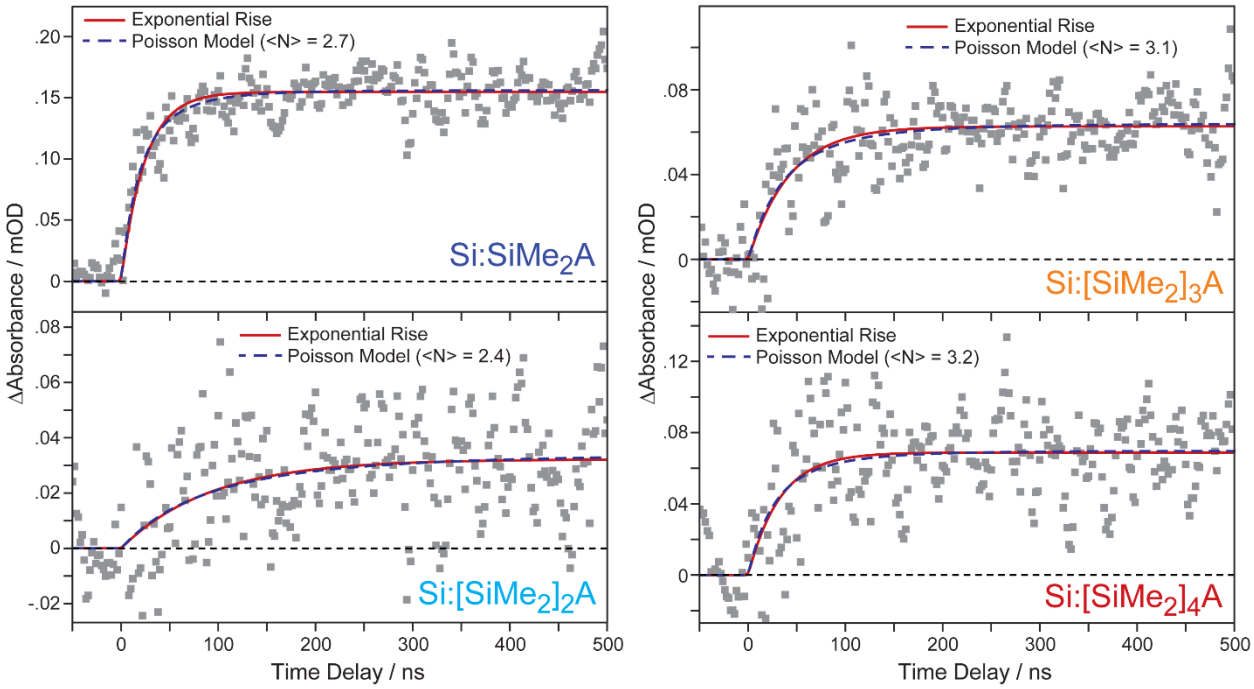

Figure S7: Triplet induced absorption rise for Si:SiMe$_2$A, Si:[SiMe$_2$]$_2$A, Si:[SiMe$_2$]$_3$A, and Si:[SiMe$_2$]$_4$A obtained by integrating TA spectra from 440 – 470 nm following removal of the Si QD background induced absorption signal. Fits to the data from an exponential rise (red) and the Poisson model (Eq. S3, blue dashed) are shown. Data reported for Si:SiMe$_2$A originally appeared in Ref. 4.

Following background subtraction, the triplet induced absorption bands of Si:SiMe$_2$A, Si:[SiMe$_2$]$_2$A, Si:[SiMe$_2$]$_3$A, and Si:[SiMe$_2$]$_4$A were integrated from 440 – 470 nm and fit to an exponential rise to determine their triplet energy transfer rates (**Figure S7**, red lines). From these fits, we determine time constants for energy transfer of 24.2 ± 3.0 ns for Si:SiMe$_2$A, 92 ± 43 ns for Si:[SiMe$_2$]$_2$A, 42 ± 9 ns for Si:[SiMe$_2$]$_3$A, and 33 ± 11 ns for Si:[SiMe$_2$]$_4$A. The error bars reported here represent one standard deviation (68% confidence interval). These fits indicate that triplet energy transfer is fastest for Si:SiMe$_2$A, slowest for Si:[SiMe$_2$]$_2$A, and intermediate for Si:[SiMe$_2$]$_3$A and Si:[SiMe$_2$]$_4$A.

We note the fitting above does not explicitly take into account slight variations in the average number of anthracene molecules that bind to the Si QDs used for each measurement. As triplet energy transfer rates are expected to increase with the number of acceptors that bind to a QD, we have also fit the rise of the triplet induced absorption signal to a model that accounts for variations in triplet transfer rates among QDs in an ensemble that bind differing numbers of triplet acceptors[4-7]. This model assumes triplet acceptors are distributed among molecules according to a Poisson distribution and that the triplet energy transfer rate for a given QD in the ensemble scales linearly with the number of acceptors it binds. This assumption yields the following functional form for the rise of the triplet induced absorption signal:

$$\boldsymbol{\Delta Abs(t) = A * \left(1 - e^{\langle N \rangle \left(e^{-k^o_{TET} t} - 1\right)}\right)} \qquad \boldsymbol{(S3)}$$

where $\boldsymbol{A}$ is a linear proportionality constant between the triplet population and strength of the TA signal, $\boldsymbol{\langle N \rangle}$ is the average number of triplet acceptors that bind to QDs in the ensemble, and $\boldsymbol{k^o_{TET}}$ is the rate for transferring a triplet exciton from an excited QD to a single molecule bound to its surface. Using values for $\boldsymbol{\langle N \rangle}$ of 2.7, 2.4, 3.1, and 3.2 for Si:SiMe$_2$A, Si:[SiMe$_2$]$_2$A, Si:[SiMe$_2$]$_3$A, and Si:[SiMe$_2$]$_4$A, respectively, that were determined from ground state absorption measurements, we find eq. S3 yields fits to the rise of the triplet induced absorption band that are of similar quality (**Figure S7** dashed blue) to the exponential fits. From these fits, we extract values for $\boldsymbol{1/k^o_{TET}}$ of 57.9 ± 7.9 ns for Si:SiMe$_2$A, 230 ± 134 ns for

Si:[$SiMe_2$]$_2$A, 120 ± 31 ns for Si:[$SiMe_2$]$_3$A, and 94 ± 37 ns for Si:[$SiMe_2$]$_4$A. Comparing these values, we still find that Si:$SiMe_2$A yields the fastest triplet energy transfer rate and Si:[$SiMe_2$]$_2$A the slowest. Hence, the rate variations we observe cannot be ascribed to differences in the number of triplet acceptors the QDs in each sample binds on average. Rather, these variations must arise from differences in the triplet energy transfer rates induced by the bridging groups of the ligands.

7. Determination of ϕ_{TET}, the efficiency of triplet energy transfer for Si:[$SiMe_2$]$_n$A

Figure S8A plots transient photoluminescence (PL) decay traces that follows the loss of far-red/near-infrared emission from Si QDs in each sample following photoexcitation. This emission decay tracks the population of photogenerated excitons that remain within the QDs as a function of time and hence reports on their survival probability. We find functionalizing the QDs with any of the H[$SiMe_2$]$_n$A ligands we investigate acts to quench the QD emission, with the largest degree of quenching occurring for Si:$SiMe_2$A and the smallest amount for Si:[$SiMe_2$]$_2$A. This degree of quenching is consistent with our TA and photon upconversion results, which show triplet energy transfer (TET) is most efficient for Si:$SiMe_2$A and least efficient for Si:[$SiMe_2$]$_2$A. If we assume the PL quenching stems purely from TET, then the difference in area underneath the normalized PL decay traces in **Figure S8A** represents the fraction of the photoexcited exciton population that has successfully undergone TET, ϕ_{TET}:

$$\phi_{TET} = \frac{\int_0^\infty \left(PL_{Si:dodecane}(t) - PL_{Si:[SiMe_2]_nA}(t)\right) dt}{\int_0^\infty PL_{Si:dodecane}(t)dt} \quad (S4)$$

Figure S8B plots the results of applying eq. S4 to the Si QD PL emission data shown in **Figure S8A**. For Si:$SiMe_2$A, we find the addition of the ligand quenches 90% of Si QD PL emission, suggesting TET is highly efficient for this system. In contrast, for Si:[$SiMe_2$]$_2$A, after a few microseconds, only ~6.6% of the Si QD emission is quenched, indicating TET is relatively inefficient for this system. Si:[$SiMe_2$]$_3$A and Si:[$SiMe_2$]$_4$A display intermediate Si QD quenching efficiencies of 61% and 55%, respectively, which is consistent with the TET rates and UCQYs seen for these systems, which are intermediate to values achieved by Si:$SiMe_2$A and Si:[$SiMe_2$]$_2$A.

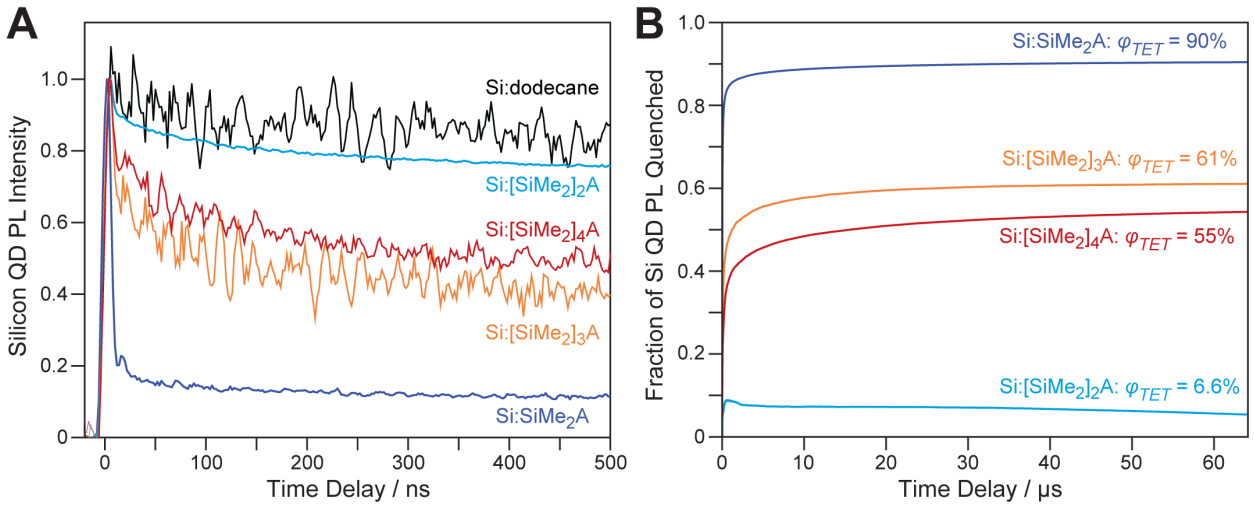

Figure S8: (A) Transient photoluminescence traces of Si:dodecane (black) compared to Si:$SiMe_2$A (blue), Si:[$SiMe_2$]$_2$A (cyan), Si:[$SiMe_2$]$_3$A (orange), and Si:[$SiMe_2$]$_4$A (red). Data recorded following photoexcitation at 532 nm at room temperature in toluene. Kinetic traces were obtained by spectrally integrating emission that arises from Si QDs from 680–780 nm. (B) Fraction of the Si QD emission that is quenched by attachment of different H[$SiMe_2$]$_n$A ligands. Plotted traces were computed using eq. S4 and their asymptotic values at long time delays reflect ϕ_{TET} under the assumption that ligand attachment only introduces a single additional Si QD exciton decay channel that stems from TET to the ligands.

III. Synthetic Procedures and Characterization of Compounds

1. General Synthesis and Characterization Information

All reactions were performed in oven-dried or flame-dried glassware, unless otherwise stated. Reaction vessels were fitted with Teflon magnetic stir bars and rubber septa, and reactions were conducted under nitrogen on a Schlenk manifold or in a nitrogen-filled glovebox. Reaction solvents were purged with argon, dried over activated alumina columns through a JC Meyer solvent purification system, and then stored over 4 Å molecular sieves. Celite plugs were conducted with Celite 545 filter aid powder. Prior to nanocrystal functionalization, the anthracenyl hydrosilanes were further purified with a LaboACE recycling preparative gel permeation chromatography system with 2HR and 2.5HR columns and *n*-hexane (HPLC grade) as the mobile phase.

Materials. 9-vinylanthracene (9VA, 97%), 9-bromoanthracene (>99.0%) and 9,10-diphenylanthracene (DPA, 98%) were purchased from TCI America. Platinum octaethylporphyrin (PtOEP, 98%) used for triplet sensitization experiments, *sec*-Butyllithium solution (*s*-BuLi, 1.4 M in cyclohexane), diisobutylaluminum hydride (DIBAL-H, 1 M in hexane) and lithium aluminum hydride ($LiAlH_4$, reagent grade, 95%), and 2,2'-Azobis(2-methylpropionitrile) (AIBN, 98%) were purchased from Sigma Aldrich. 1,2-Dichlorotetramethyldisilane ($Cl_2Si_2Me_4$, 95%) was purchased from Gelest. Deuterated chloroform ($CDCl_3$, 99.8%) and deuterated benzene (C_6D_6, 99.5%) were obtained from Cambridge Isotope Laboratories, Inc. Toluene was purchased from Fisher and dried and degassed with a JC Meyer solvent purification system. Dried methanol was procured from Sigma Aldrich and degassed before moving it into a glove box. Mesitylene (98%) was likewise obtained from Sigma Aldrich and was dried with molecular sieves. Dichlorohexamethyltrisilane ($Cl_2Si_3Me_6$) and dichlorooctamethyltetrasilane ($Cl_2Si_4Me_8$) were synthesized as previously described[8]. $HSiMe_2A$ was synthesized as previously described[4]. All chemicals were used as received.

Instrumentation. Absorption spectra were recorded on a Cary 5000 UV-Vis absorption spectrophotometer. Photoluminescence (photon upconversion) spectra were recorded on an Andor Kymera 328 spectrometer, following excitation by continuous wave (CW) solid-state lasers (488 nm: OBIS LX 75 mW). Neutral density filters (Thorlabs) were used to tune the power of the excitation source without changing its beam size. Semrock notch filters were used to remove the excitation light following the sample. Laser power was measured using a benchtop optical power and energy meter (2936R, Newport Corp.) and silicon wand detector head (818-ST2/DB, Newport Corp.).

^{1}H NMR, ^{13}C NMR, and ^{29}Si NMR were recorded on Bruker NEO400 (400 MHz), Bruker AV500 (500 MHz), or Bruker AV600 (600 MHz) spectrometers. Chemical shifts for ^{1}H NMR are reported and referenced to residual protium in NMR solvents ($CHCl_3$, δ 7.26; C_6H_6, δ 7.16). Chemical shifts for ^{13}C NMR are reported in parts per million downfield from tetramethylsilane and are referenced to the center peaks of residual solvents ($CHCl_3$, δ 77.16; C_6H_6, δ128.06). Additionally, the INEPT pulse sequence was utilized to further enhance the ^{29}Si signal through polarization transfer from ^{1}H nuclei. Chemical shifts for silicon are reported in parts per million downfield from tetramethylsilane and are referenced to a tetramethylsilane internal standard. To compensate for the low isotopic abundance of ^{29}Si, the INEPT pulse sequence was employed for amplification of the signal and determination of ^{1}H-^{29}Si coupling constants. Data are represented as follows: chemical shift, multiplicity (s = singlet, d = doublet, t = triplet, q = quartet, hept = heptet, m = multiplet), coupling constants in Hertz, and integration.

Low-resolution mass spectrometry (LRMS) was obtained via gas chromatography-mass spectrometry with an Agilent 5975 MSD with 7890A GC system, or with a Waters XEVO G3 QToF mass spectrometer equipped with a UPC2 SFC inlet, electrospray ionization (ESI) probe, atmospheric pressure chemical ionization (APCI) probe, and atmospheric solids analysis probe (ASAP).

TA measurements covering time delays of ~100 femtoseconds to a few nanoseconds were conducted using a Ti:sapphire regenerative amplifier (Coherent Legend Duo Elite, 3 kHz repetition rate, 4.5 mJ pulse

energy). A portion of the output was focused into a 5 mm thick, <001> cut CaF_2 window to generate a broadband white-light probe. Continuous translation of the CaF_2 window was employed to minimize photodamage. Another portion of the output was frequency-doubled in a Type-I β-barium borate (BBO) crystal to produce the 400 nm pump pulses. All measurements were performed using pump and probe pulses whose electric fields were oriented perpendicular to one another to suppress scattered light from contributing to the measured spectra. Samples were sealed in cuvettes and continuously stirred during acquisition to ensure homogeneity and prevent photo-degradation. A TA spectrum of toluene was recorded under identical conditions and used for dispersion and baseline correction.

TA measurements extending over nanosecond-to-millisecond time delays were conducted using an enVISion spectrometer from Magnitude Instruments that employed a 532 nm excitation laser. The repetition rate of the excitation laser was varied from 1 kHz to 19 kHz depending on the size of the delay time window scanned, with lower repetition rates used for longer time windows. TA spectra were recorded using a 2 kHz repetition rate and a pump fluence of 150 μJ/cm^2. The instrument response function for these measurements was found to give a time resolution of 4.2 ns. All silicon QD samples used for nanosecond TA measurements were prepared in a nitrogen glove box and placed into sealed cuvettes.

2. Synthesis of $H[SiMe_2]_2A$

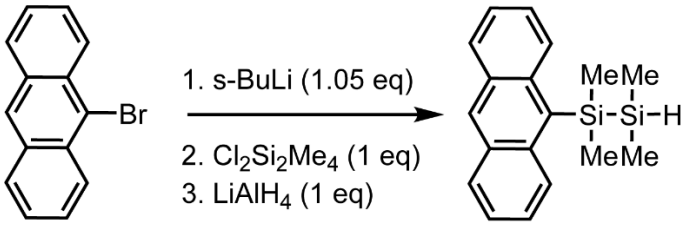

$H[SiMe_2]_2A$

An oven-dried Schlenk flask equipped with a stir bar was charged with 9-bromoanthracene (5.0 g, 19.44 mmol, 1.0 equiv.) and dissolved in THF (100 mL). *Sec*-Butyllithium (*s*-BuLi, 1.31 M, 15.33 mL, 20.41 mmol, 1.05 equiv.) was added into the reaction mixture at -78 °C, and the resulting amber mixture was stirred for 2 hours. 1,2-dichlorotetramethyldisilane ($Cl_2Si_2Me_4$, 3.62 mL, 19.44 mmol, 1.0 equiv.) was added at -78 °C and the reaction was stirred at this temperature for an additional 45 minutes before the dry ice-acetone bath was removed. The reaction mixture was allowed to warm to room temperature and stirred for 3 hours, during which the reaction mixture turned clear with a yellow tint. In a separate Schlenk flask, lithium aluminum hydride ($LiAlH_4$, 0.76 g, 20.03 mmol, 1.03 equiv.) was dissolved in 50 mL of THF. The sila-anthracene mixtures was added dropwise to the $LiAlH_4$ solution at 0 °C via cannula transfer, and the reaction was stirred at room temperature overnight. The reaction was quenched by the slow, dropwise addition of 7 mL of deionized water at 0 °C until bubbling ceased. The aqueous layer was extracted with anhydrous diethyl ether (3 × 15 mL). The combined organic layers were brine-washed, dried over sodium sulfate, then concentrated *in vacuo* to yield the crude material as a yellow solid. The crude material was dissolved in pentane and filtered through an air-free fritted funnel packed with oven-dried Celite to afford a yellow oil (2.0 g, 35% yield).

^{1}H NMR (500 MHz, $CDCl_3$) δ 8.45 (s, 1H), 8.42 – 8.37 (m, 2H), 8.05 – 7.97 (m, 2H), 7.50 – 7.40 (m, 4H), 4.02 (hept, 1H), 0.79 (s, 6H), 0.17 (d, J = 4.4 Hz, 6H). ^{13}C NMR (151 MHz, $CDCl_3$) δ 137.35, 135.09, 131.44, 129.82, 129.61, 128.92, 124.91, 124.72, 2.32, -5.56. ^{29}Si-INEPT NMR (79 MHz, $CDCl_3$) δ -23.29, -33.08 (d, J = 196.7 Hz). GC-MS: Calcd. for $C_{18}H_{22}Si_2^+$ $[M]^+$ m/z: 294.13, found m/z: 294.1.

3. Synthesis of $H[SiMe_2]_3A$

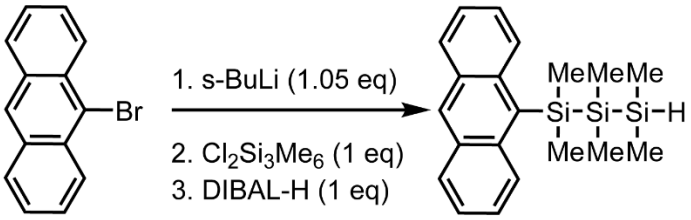

$H[SiMe_2]_3A$

An oven-dried Schenk-flask equipped with a stir bar was charged with 9-bromoanthracene (0.5 g, 1.94 mmol, 1.0 equiv.) and dissolved in THF (15 mL). Sec-Butyllithium (*s*-BuLi, 1.05 M, 1.94 mL, 2.04 mmol, 1.05 equiv.) was added into reaction mixture at -78 °C, and the resulting orange mixture was stirred for 1 hour. 1,3-dichlorohexamethyltrisilane ($Cl_2Si_3Me_6$, 0.48 g, 1.94 mmol, 1.0 equiv.) was added at -78 °C, then stirred at room temperature for 2 hours. DIBAL-H (1M in hexane, 1.94 mL, 1.94 mmol, 1 equiv.) was added at 0 °C. The reaction mixture was allowed to stir overnight at room temperature and quenched with degassed 1 M hydrochloric acid (5 mL). The aqueous layer was extracted with anhydrous diethyl ether (3 × 15 mL) and the combined organic layers were brine-washed, dried over magnesium sulfate, and then concentrated *in vacuo* to yield the crude material as a yellow solid. The crude material was purified *via* flash chromatography using aluminum oxide as the stationary phase and *n*-hexane as the eluent to yield a yellow solid (0.17 g, 25% yield).

^{1}H NMR (600 MHz, C_6D_6) δ 8.51 (d, J = 8.9 Hz, 2H), 8.20 (s, 1H), 7.82 (d, 2H), 7.35 – 7.31 (m, 2H), 7.28 – 7.23 (m, 2H), 4.04 (hept, 1H), 0.80 (s, 6H), 0.25 (s, 6H), 0.03 (d, J = 4.5 Hz, 6H). ^{13}C NMR (151 MHz, $CDCl_3$) δ 137.30, 136.18, 131.47, 129.66, 129.59, 129.20, 124.74, 124.69, 3.57, -4.85, -5.93. ^{29}Si-INEPT NMR (79 MHz, $CDCl_3$) δ -20.53, -34.12 (d, J = 91.64 Hz), -43.47. GC-MS: Calcd. for $C_{20}H_{28}Si_3^+$ $[M]^+$ m/z: 352.15, found m/z: 352.1.

4. Synthesis of $H[SiMe_2]_4A$

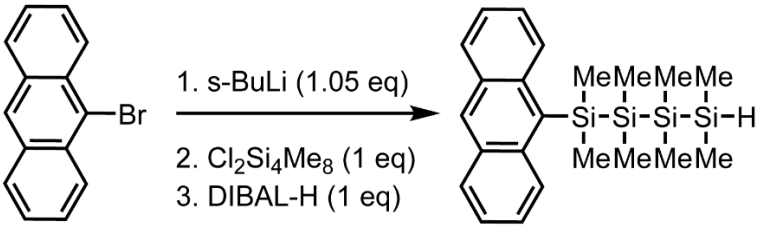

$H[SiMe_2]_4A$

An oven-dried Schenk-flask equipped with a stir bar was charged with 9-bromoanthracene (0.5 g, 1.94 mmol, 1.0 equiv.) and dissolved in THF (15 mL). *n*-BuLi (2.58 M, 0.79 mL, 2.04 mmol, 1.05 equiv.) was added into reaction mixture at -78 °C, and the resulting orange mixture was stirred for 1 hour. 1,4-dichlorooctamethyltetrasilane $Cl_2Si_4Me_8$ (0.59 g, 1.94 mmol, 1.0 equiv.) was added at -78 °C, then stirred at room temperature for 2 hours. DIBAL-H (1M in hexane, 1.94 mL, 1.94 mmol, 1 equiv.) was added at 0 °C. The reaction mixture was allowed to stir overnight at room temperature and quenched with degassed 1 M hydrochloric acid (5 mL). The aqueous layer was extracted with anhydrous diethyl ether (3 × 15 mL) and the combined organic layers were brine-washed, dried over magnesium sulfate, and then concentrated in vacuo to yield the crude material as a yellow solid. The crude material was purified *via* flash

chromatography using aluminum oxide as the stationary phase and *n*-hexane as the eluent to yield a yellow oil (0.13 g, 16% yield).

^{1}H NMR (600 MHz, C_6D_6) δ 8.52 (d, J = 8.9 Hz, 2H), 8.21 (s, 1H), 7.83 (d, J = 8.3 Hz, 2H), 7.37 – 7.31 (m, 2H), 7.29 – 7.23 (m, 2H), 3.99 (hept, J = 4.6 Hz, 1H), 0.82 (s, 6H), 0.33 (d, J = 0.9 Hz, 6H), 0.11 – 0.05 (m, 12H). ^{13}C NMR (151 MHz, C_6D_6) δ 137.59, 136.19, 131.77, 130.03, 129.76, 129.25, 124.74, 124.65, 3.97, -4.13, -5.89, -6.02. ^{29}Si-INEPT NMR (79 MHz, C_6D_6) δ -19.81, -36.32 (d, J = 194.5 Hz), -40.79, -43.65. LR-MS (ASAP): Calcd. for $C_{22}H_{34}Si_4^+$ $[M]^+$ m/z: 410.1, found m/z: 410.1.

5. NMR of $H[SiMe_2]_2A$, $H[SiMe_2]_3A$ and $H[SiMe_2]_4A$

NMR Spectra of $H[SiMe_2]_2A$

^1H NMR Spectrum (500 MHz, $CDCl_3$):

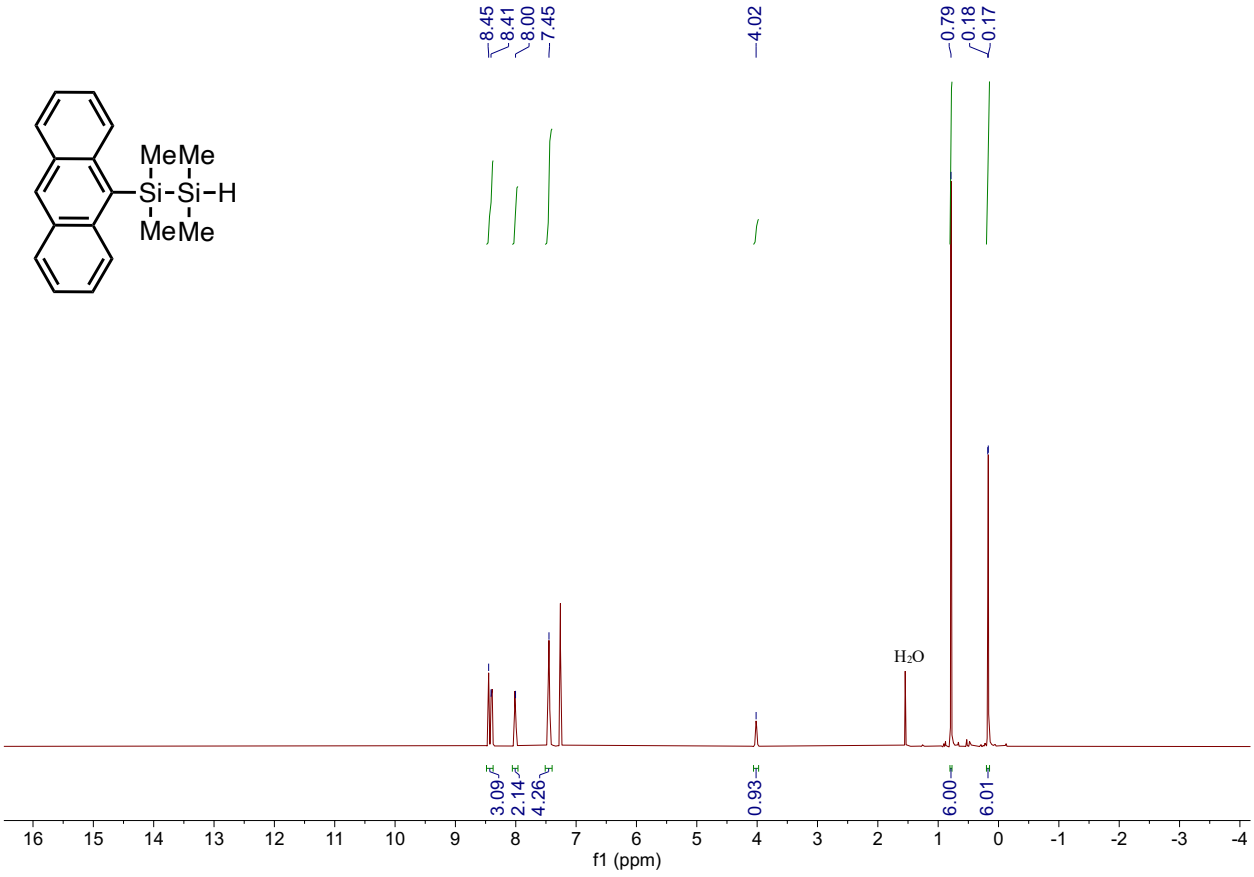

$^{13}C\{^{1}H\}$ NMR Spectrum (101 MHz, $CDCl_3$):

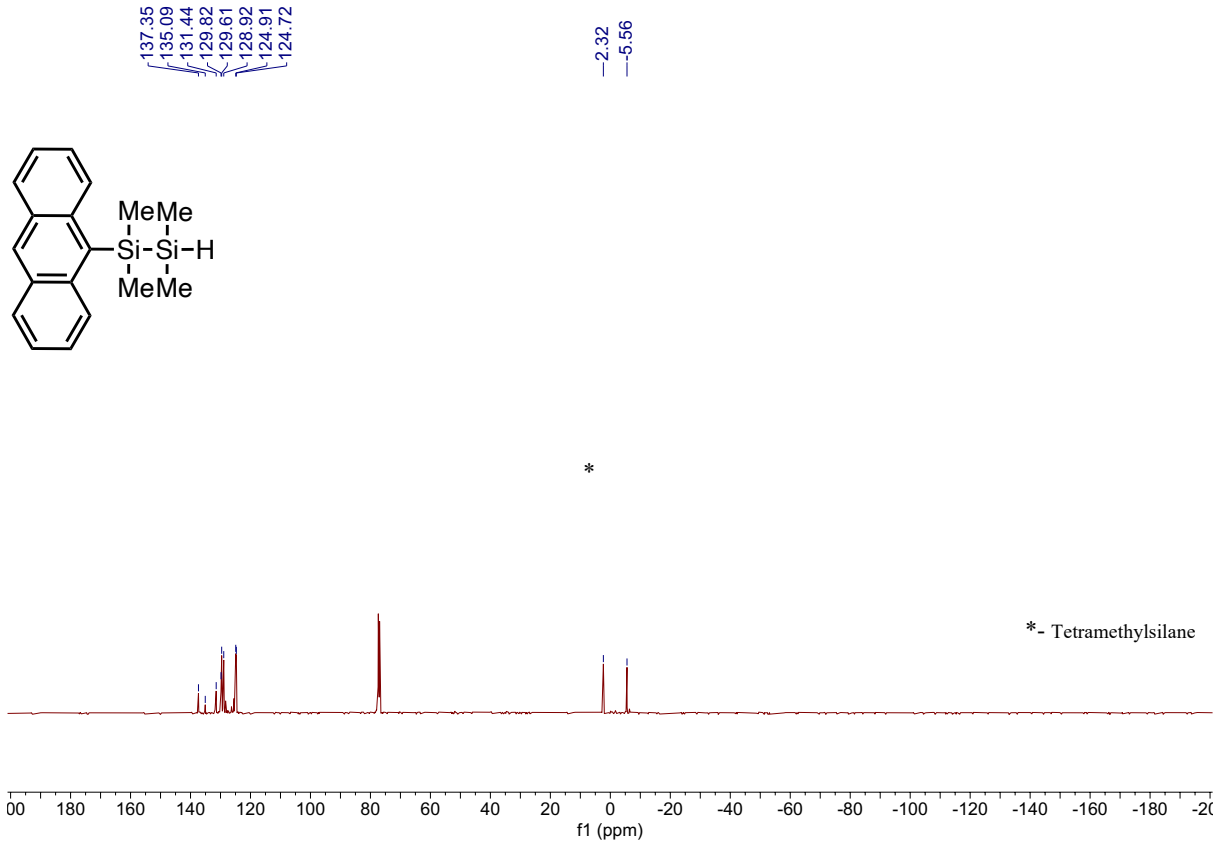

^{29}Si-INEPT NMR Spectrum (79 MHz, $CDCl_3$):

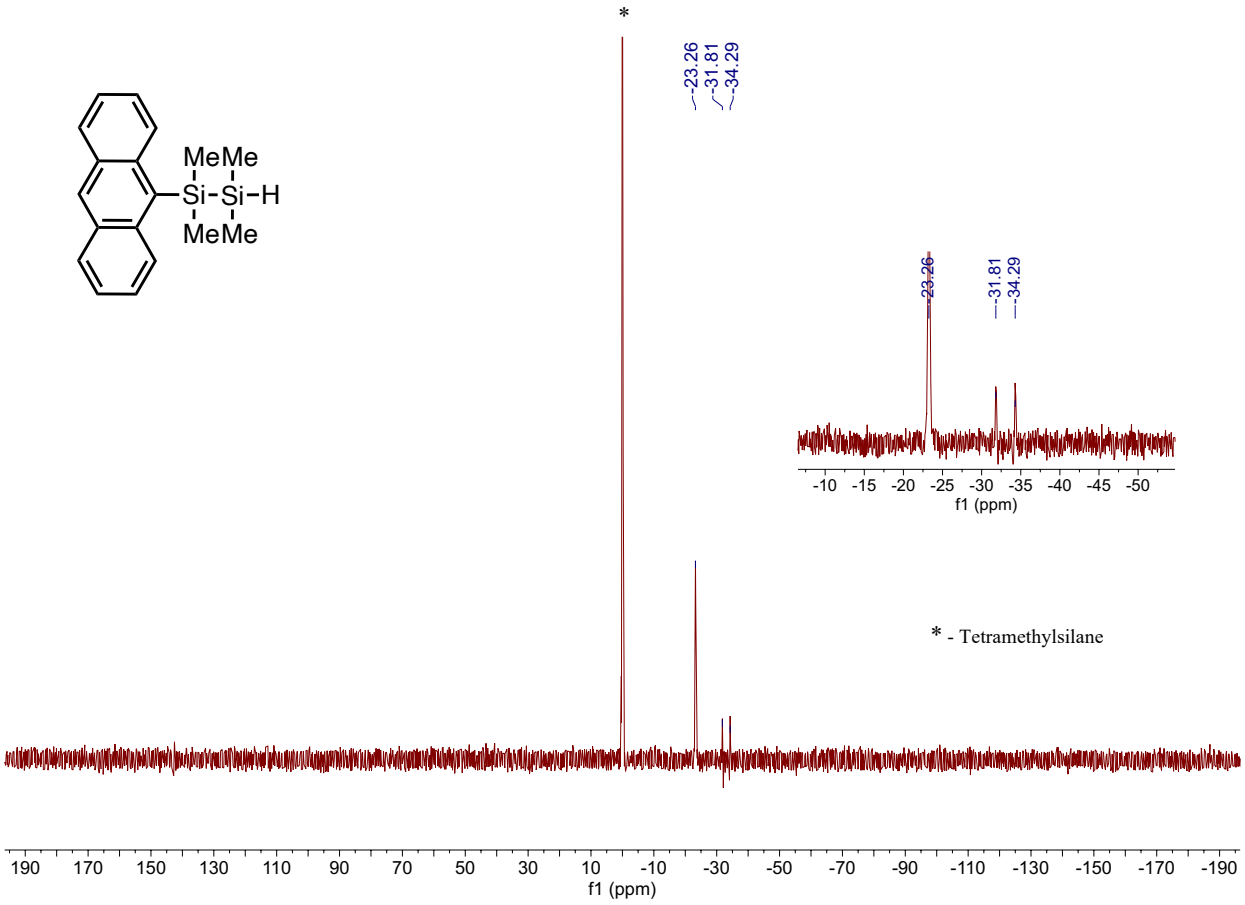

NMR Spectra of H[SiMe$_2$]$_3$A

^{1}H NMR Spectrum (600 MHz, C_6D_6):

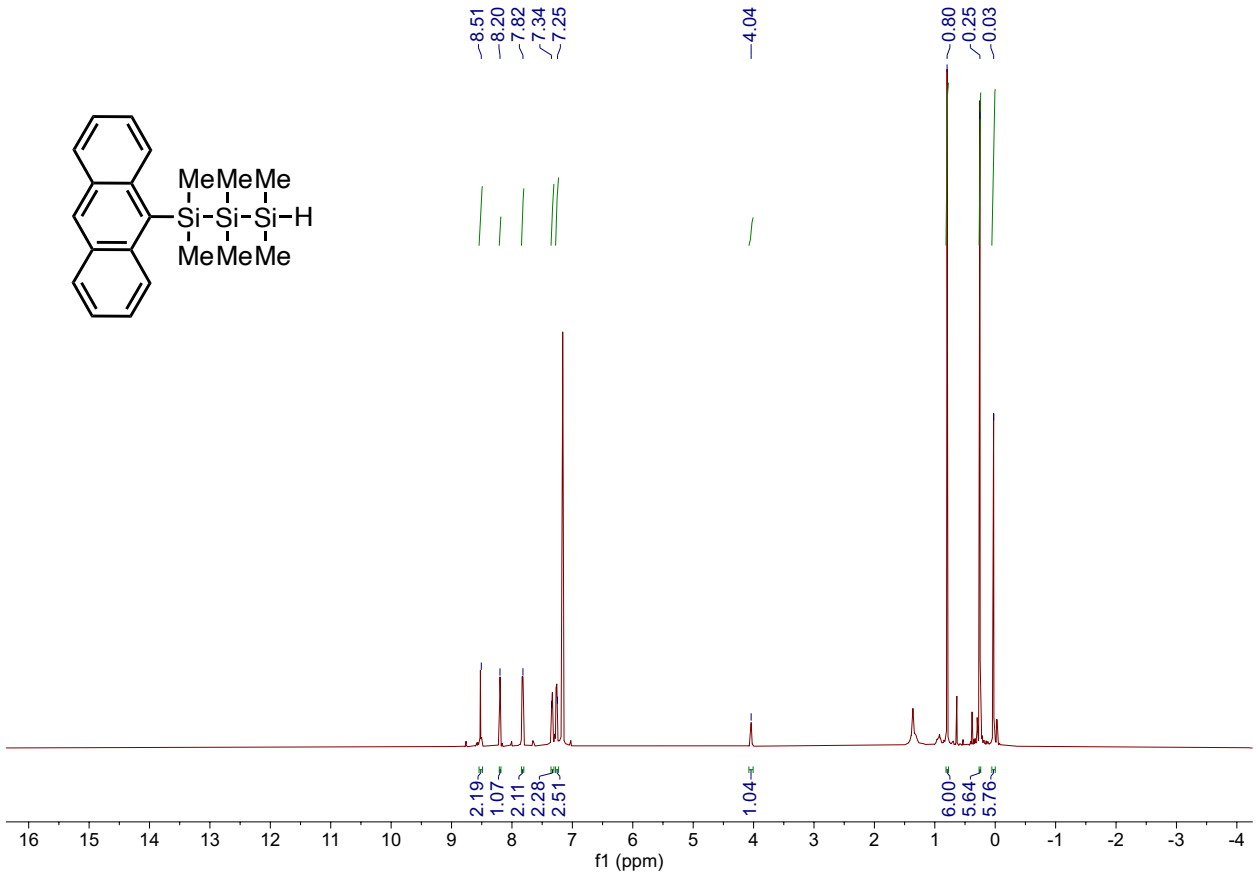

$^{13}C\{^{1}H\}$ NMR Spectrum (151 MHz, $CDCl_3$):

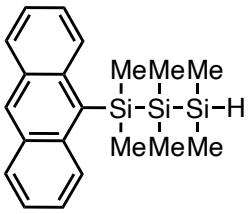

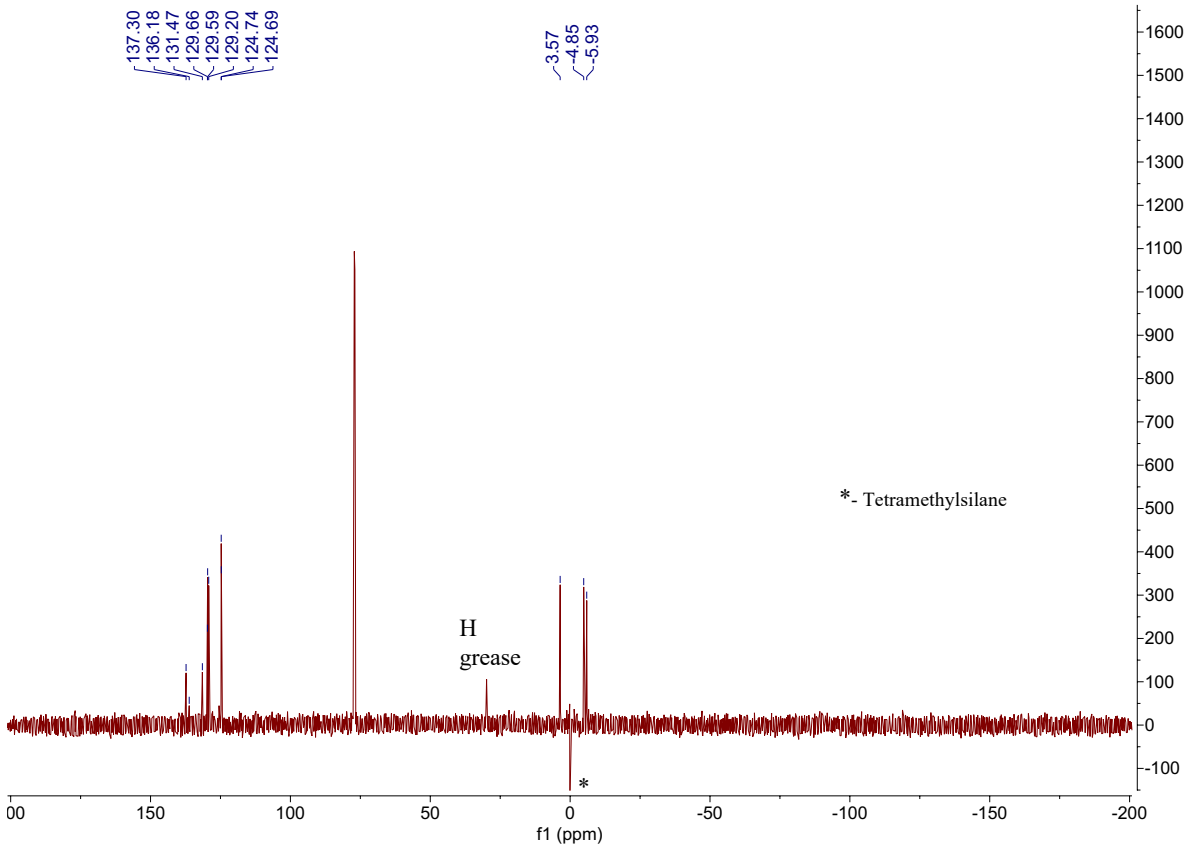

^{29}Si-INEPT NMR Spectra (79 MHz, C_6D_6):

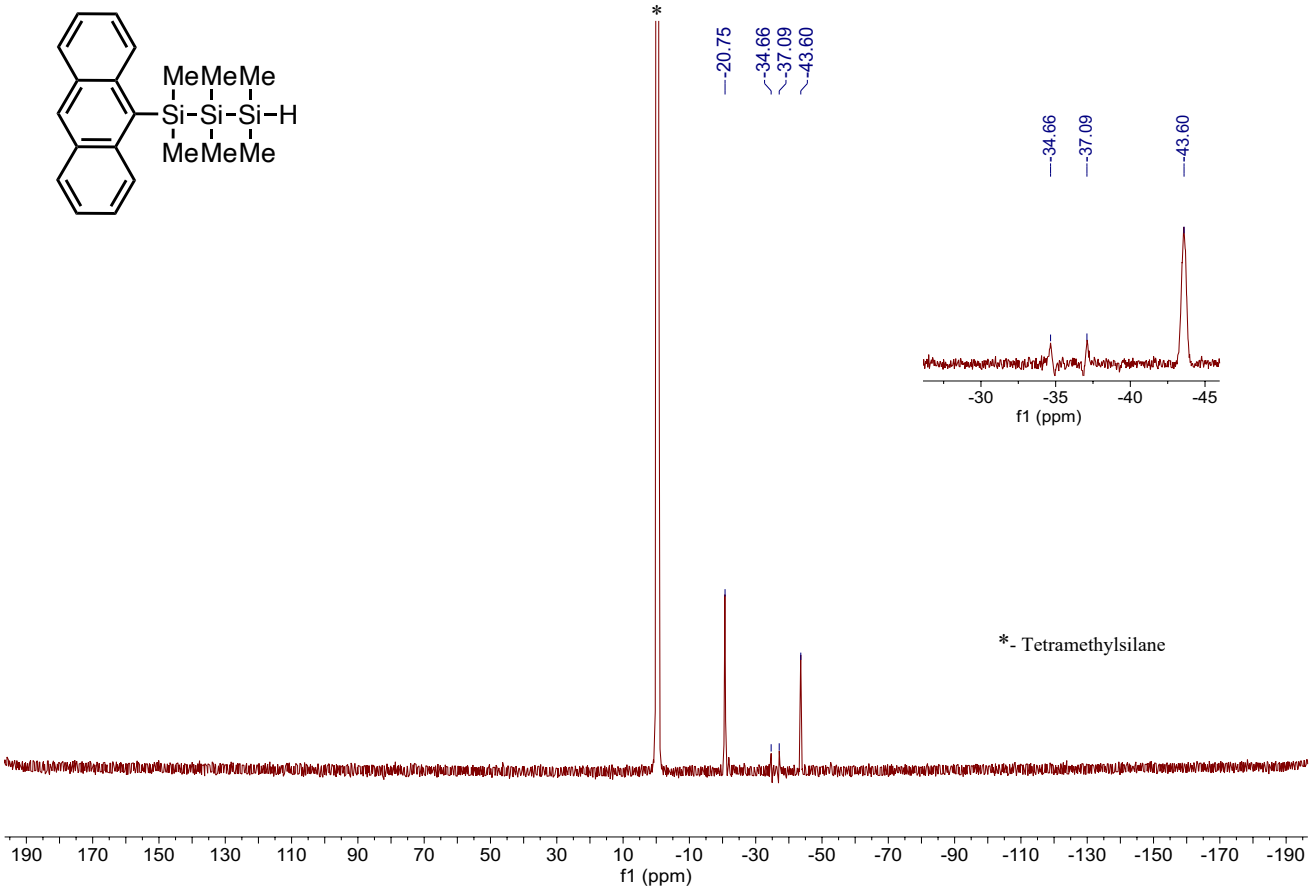

NMR Spectra of H[SiMe$_2$]$_4$A

^{1}H NMR Spectrum (600 MHz, C_6D_6):

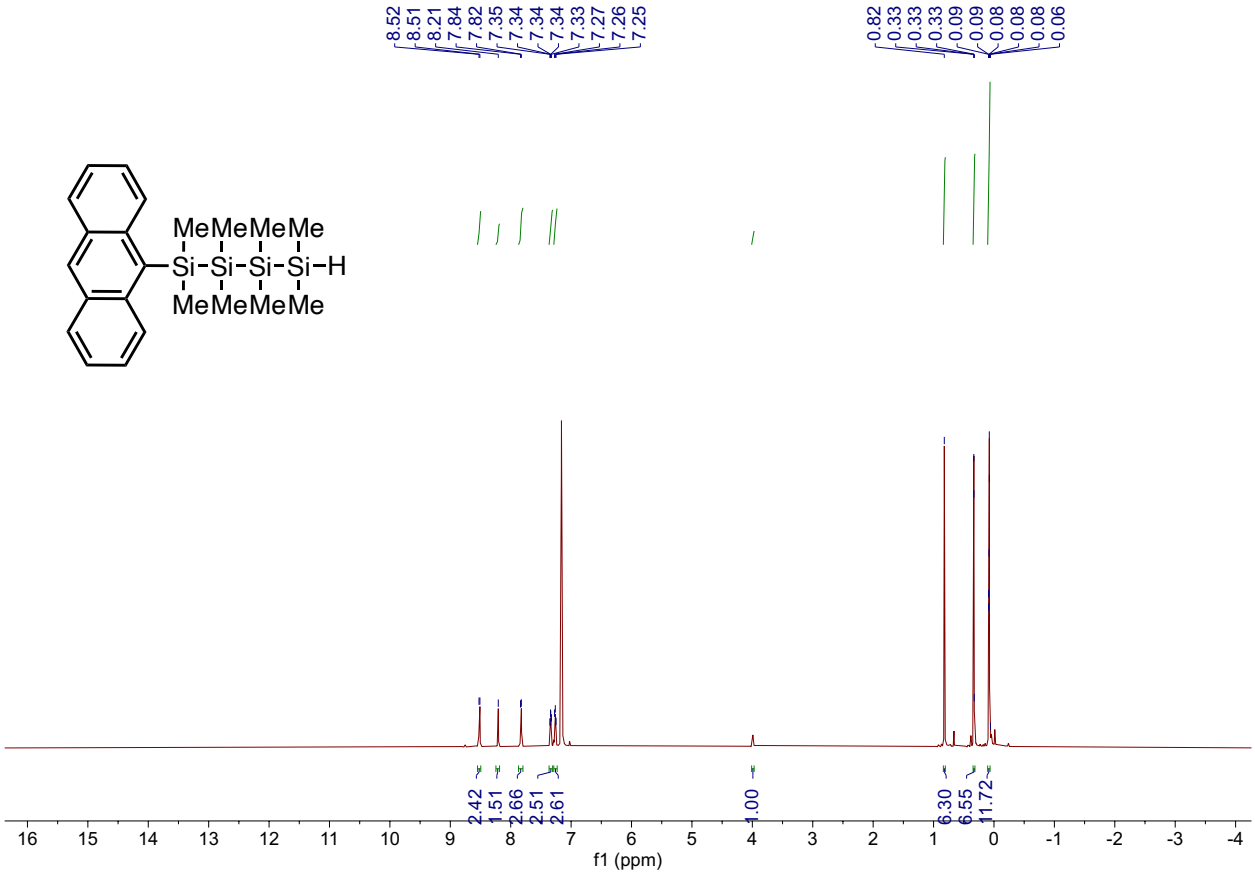

$^{13}C\{^{1}H\}$ NMR Spectrum (151 MHz, C_6D_6):

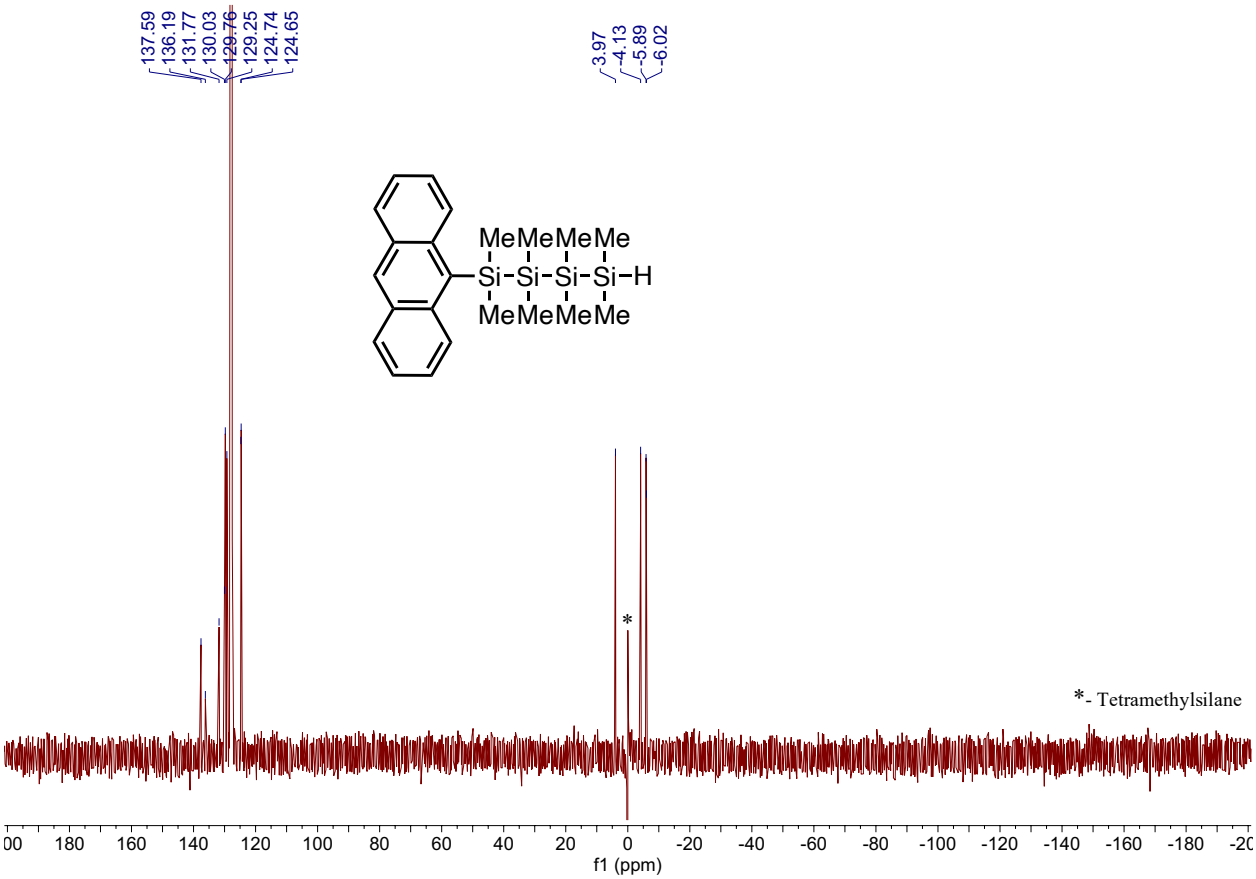

^{29}Si INEPT NMR Spectrum (79 MHz, C_6D_6):

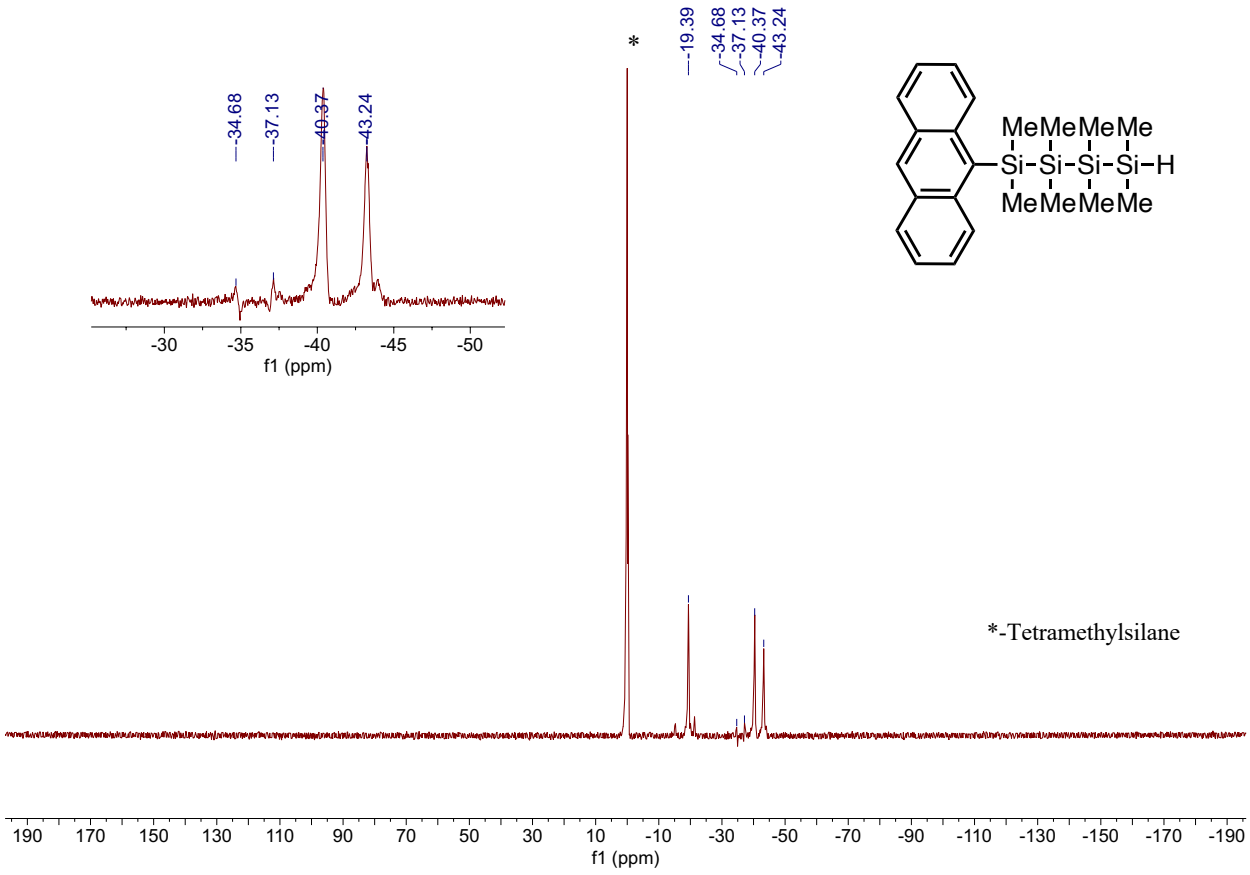

IV. Computational Methods

1. Electronic Structure Details

We model the Si:[$SiMe_2$]$_n$A (n = 1 – 4) systems identically to our previous work[9]. Briefly, we model the QD with a silicon slab that is six layers thick in the z-direction and has four silicon unit cells in each of the x- and y-directions (**Figure S8**). We include approximately 20 Å of vacuum in the z-direction, forming a (111) facet on each side of the silicon slab—the most stable facet that will appear on a Si QD. The vacuum ensures the system is 'semi'-periodic and does not interact with its replica in the z-direction. We attach the [$SiMe_2$]$_n$A (n = 1 – 4) ligand to the center of one side of the slab and passivate other dangling silicon bonds with pseudo hydrogens.

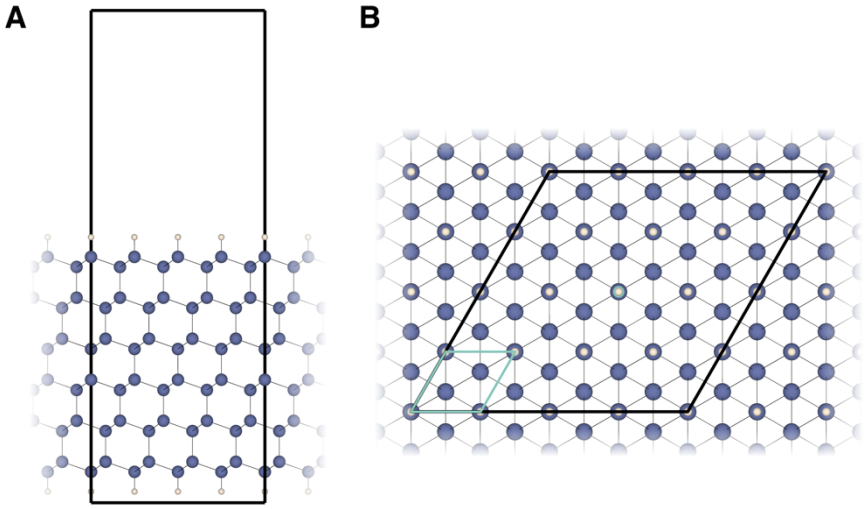

Figure S9: The bare silicon slab used to represent a Si QD. The slab is 6 crystalline Si unit cells thick (A) with approximately 20 Å of vacuum. The hexagonal supercell (B) is made up of 4×4 crystalline Si unit cells (one outlined in light blue). The center hydrogen (highlighted by a light blue circle) is replaced with the desired ligand and vacuum is added to maintain distance between the attached ligand and the repeated slab.

We use density functional theory (DFT) as implemented in the Vienna Ab-initio Simulation Package (VASP) to investigate the electronic structure of the Si:[$SiMe_2$]$_n$A (n = 1 – 4) systems (**Figure S9**)[10]. To ensure consistency in our results, we maintain the same computational parameters as used in our previous work and repeat the details here[4]. All of our calculations use the projector augmented wave (PAW) method to describe the atomic potentials and the generalized gradient approximation (GGA) method of Perdew-Burke-Ernzerhof (PBE) for the exchange-correlation functional[11]. Dispersion corrections were treated using the DFT-D3 method with the Becke-Johnson damping function and dipole and quadrupole corrections were added in the direction of the vacuum (z-direction)[12]. As is described in our previous work and briefly in the main text, the triplet excited states are found by allowing spin-polarization and finding the lowest-energy triplet state.

For the more expensive geometry relaxations, we converged the minimum energy to 10^{-5} eV using a 540 eV plane-wave cutoff, a 3×3×1 k-point grid, and partial occupancies described using Gaussian smearing with a smearing width of 0.01 eV. We freeze the central silicon atoms in the slab at their bulk geometry and relax the rest of the slab and a-top molecule until the maximum force in any direction on any free-moving atom is less than 10 meV/Å.

Following geometry optimization, we perform a single self-consistent energy calculation using an energy convergence of 10^{-7} eV, a 7×7×1 k-point grid, and partial occupancies set using the tetrahedron method with Blöchl corrections. The resulting charge density and wavefunction we find are used to compute the density of states (DOS) for the spin-up and spin-down triplet components. We convolve the DOS of these two channels to obtain the exciton DOS shown in the main text. The choice of k-point sampling grid

is restricted to 7×7×1 as more dense sampling grids are computationally infeasible. Based on the computed FWHM values at a 6×6×1 sampling, the FWHM error due to convergence is 0.01 eV to the nearest order of magnitude.

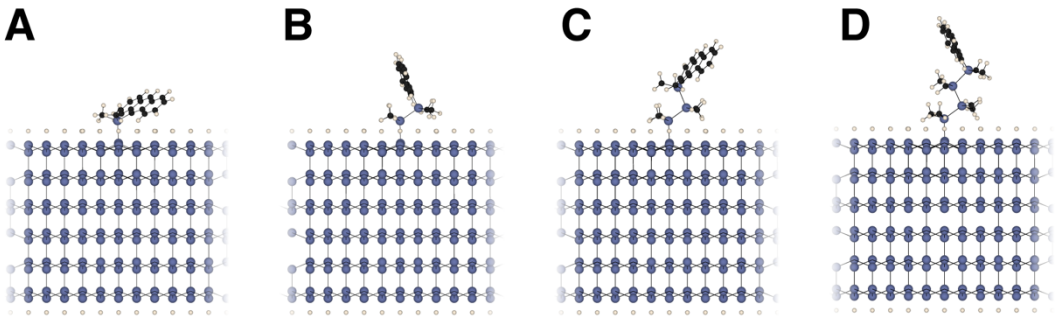

Figure S10: The Si:$[SiMe_2]_n$A systems are optimized in VASP to find their electronic ground states, shown here for (A) Si:$SiMe_2$A, (B) Si:$[SiMe_2]_2$A, (C) Si:$[SiMe_2]_3$A, and (D) Si:$[SiMe_2]_4$A. We have hidden the outline of the supercell so it does not obscure the side profile of the chains.

2. Classical Dynamics Simulations

We explored dynamical motion of the ligand chains using a full QD model (**Figure S10**). The QD was formed by cutting a sphere with the appropriate diameter (about 30 Å) from bulk silicon and passivating dangling bonds with hydrogen. We found a (111) facet of the sphere and attached the ligand to the center of this face. Using this model, we ran 500 ps of dynamics with 0.5 fs timesteps at a temperature of 300 K using the ReaxFF potential as implemented in LAMMPS[13, 14].

We track the degree of bending in the chain with the radius of gyration, often used to describe polymer folding:

$$R_g = \sqrt{\sum_i^N m_i(r_i - r_{CM})^2 / M} \qquad (S5)$$

where r_{CM} is the center of mass of all the atoms, M is the total mass of atoms in the chain, and m_i and r_i is the mass and position of atom i in the chain, respectively. We define the chain as the silicon within the QD that the chain is attached to, each silicon atom within the chain, and the carbon atoms in the anthracene at the 9 and 10 positions. Si:$SiMe_2$A experiences large fluctuations of its R_g. Because there is only one silicon atom in the chain, we attribute all fluctuations to the anthracene molecule swaying between a position more face down on the silicon QD (**Figure S10A**) and a position perpendicular to the silicon QD. Si:$[SiMe_2]_2$A is, in contrast, quite rigid and has no detectable configurational switches. Si:$[SiMe_2]_n$ (n = 3, 4) have two clear configurational states (**Figure 10C-F**) that are driven by the dimethylsilane chain stretching itself into a more linear or more curved shape. The curved configuration brings the anthracene molecule close to the Si QD surface.

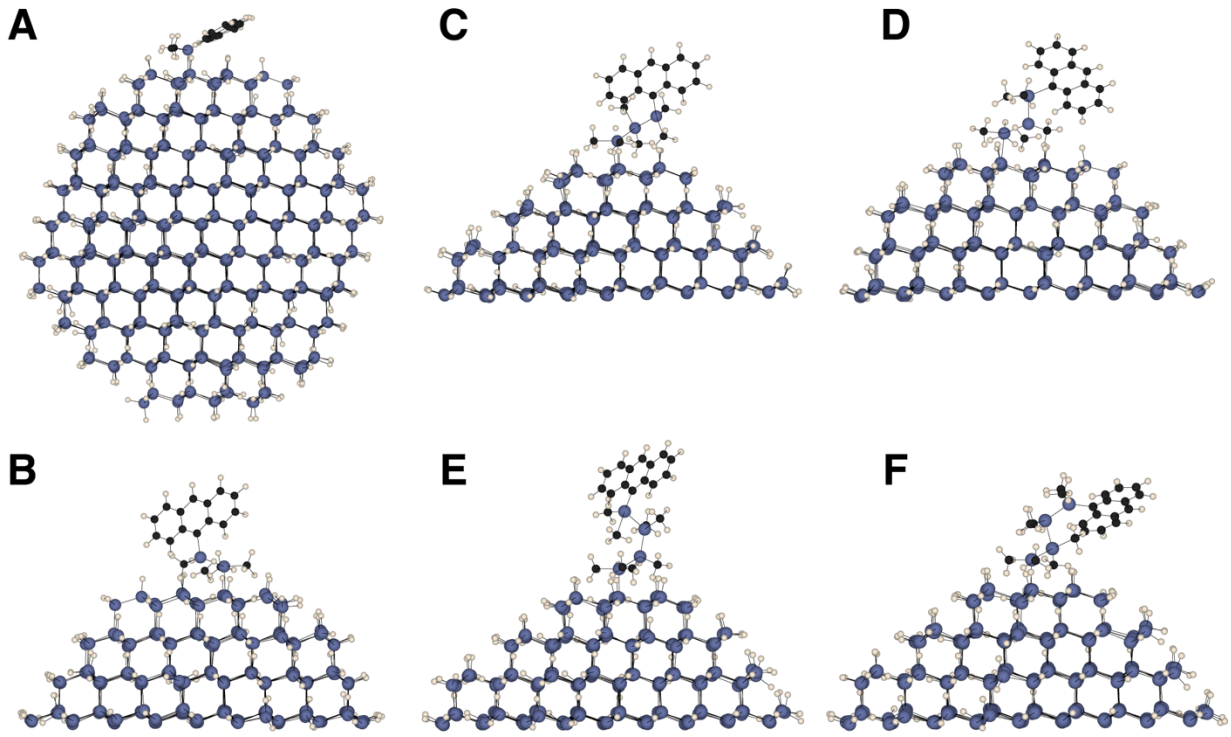

Figure S11: Snapshots of the Si:[$SiMe_2$]$_n$A systems from classical dynamics in LAMMPS. We model the full 30 Å diameter QD as seen in the (A) Si:$SiMe_2$A system and attach the [$SiMe_2$]$_n$A chain to one of the (111) terminated surfaces. (A) Si:$SiMe_2$A and (B) Si:[$SiMe_2$]$_2$A predominately stay in the given configurations and do not exhibit large conformational changes at 300 K. (C-D) Si:[$SiMe_2$]$_3$A, and (E-F) Si:[$SiMe_2$]$_4$A find two distinct conformations as shown here. These systems may remain in one configuration for tens to hundreds of picoseconds before spontaneously flipping to the other configuration throughout the simulation.

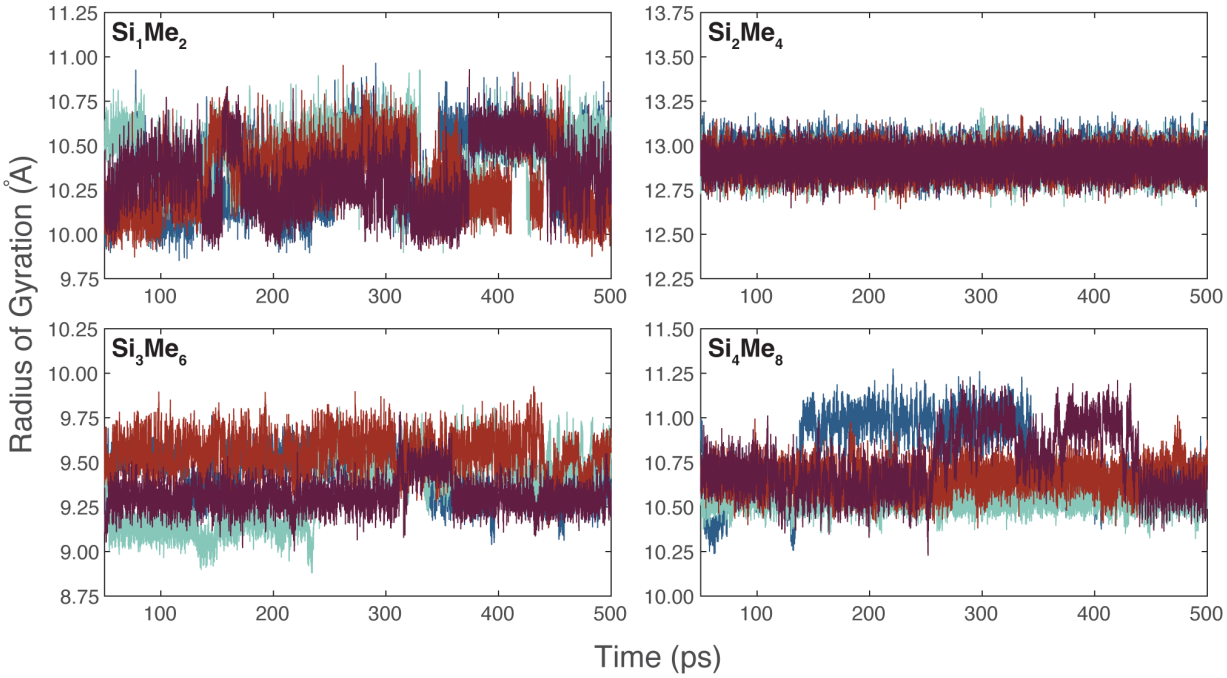

Figure S12: The radius of gyration R_g during four trajectories at 300 K for Si:$[SiMe_2]_n$A. The jumps signal a large conformational change in the chain. Notably, Si:$[SiMe_2]_2$A doesn't exhibit any jumps during any of the trajectories, while the others exhibit fluctuations around two different R_g values for several picoseconds at a time. This is due to steric interactions from the attached methyl groups. The longer chains can work around these steric interactions to bend significantly. Trajectory 4, dark maroon above, is used to create representative video samples, described below.

3. MPEG files

All videos are taken at 50 fs step sizes for a length of approximately 50 ps to limit file size.

- $[SiMe_2]_n$:A (n = 1-4) – first 50 ps of trajectory 4, which is taken as equilibration time
- $[SiMe_2]_n$:A (n = 1-4) – first 50 ps post equilibration time for trajectory 4
- $[SiMe_2]_1$:A – 350 ps to 400 ps of trajectory 4
- $[SiMe_2]_3$:A – 300 ps to 350 ps of trajectory 4
- $[SiMe_2]_4$:A – 250 ps to 300 ps of trajectory 4

IV. References

(1) Xia, P.; Raulerson, E. K.; Coleman, D.; Gerke, C. S.; Mangolini, L.; Tang, M. L.; Roberts, S. T. Achieving spin-triplet exciton transfer between silicon and molecular acceptors for photon upconversion. *Nat. Chem.* **2020**, *12* (2), 137–144. DOI: 10.1038/s41557-019-0385-8.

(2) Roberts, S. T.; Schlenker, C. W.; Barlier, V.; McAnally, R. E.; Zhang, Y. Y.; Mastron, J. N.; Thompson, M. E.; Bradforth, S. E. Observation of Triplet Excito Formation in a Platinum-Sensitized Organic Photovoltaic Device. *J. Phys. Chem. Lett.* **2011**, *2* (2), 48–54. DOI: 10.1021/jz101554m.

(3) Baldo, M.; O'Brien, D.; You, Y.; Shoustikov, A.; Sibley, S.; Thompson, M.; Forrest, S. Highly efficient phosphorescent emission from organic electroluminescent devices. *Nature* **1998**, *395* (6698), 151–154. DOI: 10.1038/25954.

(4) Nguyen, N.; Lewis, S.; Wang, K.; Wang, H.; Gonzalez, A.; Mangolini, L.; Roberts, S.; Tang, M.; Eaves, J.; Su, T. Intermediate Electronic Coupling via Silane and Germane Bridges in Silicon Quantum Dot-Molecular Hybrid Systems. *Nano Lett.* **2025**, *25* (13), 5299–5306. DOI: 10.1021/acs.nanolett.5c00169.

(5) Cadena, D.; Sowa, J.; Cotton, D.; Wight, C.; Hoffman, C.; Wagner, H.; Boette, J.; Raulerson, E.; Iverson, B.; Rossky, P.; et al. Aggregation of Charge Acceptors on Nanocrystal Surfaces Alters Rates of Photoinduced Electron Transfer. *J. Am. Chem. Soc.* **2022**, *144* (49), 22676–22688. DOI: 10.1021/jacs.2c09758.

(6) Morris-Cohen, A. J.; Frederick, M. T.; Cass, L. C.; Weiss, E. A. Simultaneous Determination of the Adsorption Constant and the Photoinduced Electron Transfer Rate for a Cds Quantum Dot–Viologen Complex. *J. Am. Chem. Soc.* **2011**, *133* (26), 10146–10154. DOI: 10.1021/ja2010237.

(7) Utterback, J. K.; Wilker, M. B.; Brown, K. A.; King, P. W.; Eaves, J. D.; Dukovic, G. Competition between electron transfer, trapping, and recombination in CdS nanorod–hydrogenase complexes. *Phys. Chem. Chem. Phys.* **2015**, *17* (8), 5538–5542, 10.1039/C4CP05993J. DOI: 10.1039/C4CP05993J.

(8) Su, T.; Li, H.; Steigerwald, M.; Venkataraman, L.; Nuckolls, C. Stereoelectronic switching in single-molecule junctions. *Nat. Chem.* **2015**, *7* (3), 215–220. DOI: 10.1038/nchem.2180.

(9) Wang, K. F.; Cline, R. P.; Schwan, J.; Strain, J. M.; Roberts, S. T.; Mangolini, L.; Eaves, J. D.; Tang, M. L. Efficient photon upconversion enabled by strong coupling between silicon quantum dots and anthracene. *Nat. Chem.* **2023**, *15* (8), 1172–1178. DOI: 10.1038/s41557-023-01225-x.

(10) Kresse, G.; Furthmuller, J. Efficient iterative schemes for ab initio total-energy calculations using a plane-wave basis set. *Phys. Rev. B* **1996**, *54* (16), 11169–11186. DOI: 10.1103/PhysRevB.54.11169.

(11) Kresse, G.; Joubert, D. From ultrasoft pseudopotentials to the projector augmented-wave method. *Phys. Rev. B* **1999**, *59* (3), 1758–1775. DOI: 10.1103/PhysRevB.59.1758.

(12) Grimme, S.; Ehrlich, S.; Goerigk, L. Effect of the Damping Function in Dispersion Corrected Density Functional Theory. *J. Comput. Chem.* **2011**, *32* (7), 1456–1465. DOI: 10.1002/jcc.21759.

(13) Thompson, A.; Aktulga, H.; Berger, R.; Bolintineanu, D.; Brown, W.; Crozier, P.; Veld, P.; Kohlmeyer, A.; Moore, S.; Nguyen, T.; et al. LAMMPS-a flexible simulation tool for particle-based materials modeling at the atomic, meso, and continuum scales. *Comput. Phys. Commun.* **2022**, *271*. DOI: 10.1016/j.cpc.2021.108171.

(14) Chenoweth, K.; van Duin, A.; Goddard, W. ReaxFF reactive force field for molecular dynamics simulations of hydrocarbon oxidation. *J. Phys. Chem. A* **2008**, *112* (5), 1040–1053. DOI: 10.1021/jp709896w.